Revision #1

Thermodynamic, elastic and vibrational (IR/Raman) behaviour of mixed type-AB carbonated hydroxylapatite by density functional theory

Gianfranco Ulian*, Daniele Moro and Giovanni Valdrè*

Dipartimento di Scienze Biologiche, Geologiche e Ambientali, Centro di Ricerche Interdisciplinari di Biomineralogia, Cristallografia e Biomateriali, Università di Bologna "Alma Mater Studiorum" Piazza di Porta San Donato 1, 40126 Bologna, Italy

* Corresponding authors: giovanni.valdre@unibo.it ; gianfranco.ulian2@unibo.it

Abstract

The present investigation reports the equation of state, thermodynamic and thermoelastic properties of type AB carbonated apatite [CAp-AB, $Ca_{10}(CO_3)^B(PO_4)_5(CO_3)^A$, space group $P1$], as obtained from Density Functional Theory simulations and the quasi-harmonic approximation. The static (0 K) third-order Birch-Murnaghan equation of state resulted in the parameters K_0 = 104.3(8) GPa, K' = 4.3(1) and V_0 = 517.9(2) Å^3, whereas at room temperature (300 K) they were K_T = 101.98 GPa, K' = 4.12 and V_0 = 524.486 GPa. Thermodynamics and thermoelasticity were calculated in the temperature range 0 – 800 K and between 0 GPa and 30 GPa.

Furthermore, the dependence of the infrared/Raman spectra of type-AB carbonated apatite with pressure is also reported, which could be useful for researchers interested in vibrational spectroscopy. The theoretical results corroborate the few experimental ones on a similar type AB carbonated hydroxylapatite, and provide further details over wide pressure and temperature ranges on the elastic, thermodynamic and infrared/Raman properties of this important mineral found in both geological and biological environments.

Keywords: Type AB carbonated apatite, thermodynamic properties, elastic properties, Density Functional Theory, quasi-harmonic approximation.

This is the peer-reviewed, final accepted version for American Mineralogist, published by the Mineralogical Society of America.
The published version is subject to change. Cite as Authors (Year) Title. American Mineralogist, in press.
DOI: https://doi.org/10.2138/am-2021-7826. http://www.minsocam.org/

INTRODUCTION

Since the pioneering work of Albee in the first half of the 20th century (Albee, 1920), a continuous and still growing interest towards the role of hydroxylapatite [OHAp, $Ca_{10}(PO_4)_6(OH)_2$] as the mineral component of bone tissues has been recorded in scientific literature. The main goal of all the fundamental and applied researches is the development of a biomaterial for bone and tooth repair, reconstruction, and replacement. OHAp is found in bony tissues in its hexagonal polymorph (space group $P6_3/m$), presenting a calcium channel with two hydroxyl groups oriented in the same direction along the **c**-axis. However, from the thermodynamics point of view, hexagonal hydroxylapatite is less stable than its monoclinic phase (space group $P2_1/b$) commonly found in igneous rocks, which is explained by the different OH alignment in the apatite channel. The monoclinic/hexagonal transition have been evaluated to occur at 200 °C at ambient pressure (Suda et al., 1995).

It is a well-established fact that bony tissues do not contain stoichiometric hydroxylapatite, but the so-called "bone apatite", a mineral presenting a complex crystal-chemistry with general formula (Ca, X)$_{10}$(PO$_4$, Y)$_6$(OH, Z)$_2$, where X = Na^+, Mg^{2+}, Pb^{2+} represents some cationic substitution and Y and Z anionic ones, such as CO_3^{2-} (Dorozhkin, 2009). In addition, even neutral molecules, such as water, may enter in the mineral structure. As mentioned, among the several possible anionic substitutions, carbonate ion ones represent the most common, accounting for up to about 6 wt.% in bone mineral. Depending on the crystal site occupied by the carbonate anion, the substitution is called type-A if involves the hydroxyl groups (Z):

$$2OH^-_{(cell)} + CO_3^{2-} \rightarrow CO^{2-}_{3(cell)} + 2OH^-$$

The above reaction accounts for the charge neutrality of the system by considering the removal of an additional OH^- from the hexagonal calcium channel. The second substitution, called type-B, involves the removal of a phosphate ion (Y), according to:

$$PO^{3-}_{4(cell)} + CO_3^{2-} \rightarrow CO^{2-}_{3(cell)} + PO_4^{3-}$$

This is the peer-reviewed, final accepted version for American Mineralogist, published by the Mineralogical Society of America.
The published version is subject to change. Cite as Authors (Year) Title. American Mineralogist, in press.
DOI: https://doi.org/10.2138/am-2021-7826. http://www.minsocam.org/

Differently from type-A substitutions, the type-B ones lead to charge unbalance in the mineral. Several hypotheses were advanced to restore the neutrality of the unit cell (Peroos et al., 2006), but one of most probable is related to the following reaction:

$$PO^{3-}_{4(cell)} + Ca^{2+}_{(cell)} + CO^{2-}_{3} + M^{+} \rightarrow CO^{2-}_{3(cell)} + M^{+}_{(cell)} + PO^{3-}_{4} + Ca^{2+}$$

where the formation of the type-B defect is accompanied by the substitution of a divalent calcium ion with a monovalent one, such as sodium in biological environment as reported by Dorozhkin (Dorozhkin, 2009; Dorozhkin, 2010; Dorozhkin, 2011). However, it is worth noting that, in nature, carbonate ion is commonly found in a mixed type-AB carbonated hydroxylapatite (COHAp).

Several experimental (Fleet and Liu, 2003; Fleet and Liu, 2004; Fleet et al., 2004; Fleet and Liu, 2007; Fleet and Liu, 2008; Fleet, 2009; Fleet et al., 2011) and theoretical (Peeters et al., 1997; Astala and Stott, 2005; Peroos et al., 2006; Rabone and de Leeuw, 2007; Ulian et al., 2013a; Peccati et al., 2014; Ulian et al., 2014) works were devoted to the structural analysis of bulk type-A, type-B and type-AB carbonated (hydroxyl)apatites, focusing on the position and orientation of the carbonate ion within the unit cell. In addition, more recent researches were involved in the characterization of the surface properties (morphology, electrostatic surface potential, adsorption features) of COHAp, to increase the fundamental knowledge on this mineral family and reach a better understanding of the mineral/biological environment interaction phenomena (de- and remineralization, reconstruction, simple and complex biomolecule adsorption, such as peptides, proteins, lipids, etc.) for its employment in biomaterial applications.

However, while the structural and surface features of carbonated hydroxylapatite are of utmost importance for obtaining biomaterials with improved biocompatibility/bioactivity, they are not enough if the goal is creating fully fledged prosthetics for support function (*e.g.* hip implants). For this application, the elastic properties of the biomaterial, related to the crystal-chemistry of the carbonated hydroxylapatite, have to be known in detail. Some efforts in this sense started in the last decade, for example calibrated Raman piezo-spectroscopy was employed to investigate the microscopic processes governing the mechanical behaviour of bone tissues in sane and osteoporotic

rats, to better understand how the pathology affects the physical properties of the tissue (Pezzotti et al., 2017).

From the experimental point of view, powder X-ray diffraction experiments were conducted up to 10 GPa at room temperatures (ca. 300K) on two samples of type-AB carbonated hydroxylapatite to obtain the equation of state of the mineral (Liu et al., 2011). A related third-order Birch-Murnaghan equation of state showed that the bulk modulus of the mineral lies between 73(2) GPa and 87(2) GPa depending on the crystal-chemistry of the carbonated hydroxylapatite. The highest elastic stiffness was observed when almost all hydroxyl groups were substituted by carbonate ions. Very recently, a Density Functional Theory (DFT) investigation was performed on a type-A carbonated apatite (CAp), with chemical formula $Ca_{10}(PO_4)_6CO_3$, showing similarities in the elastic behaviour with those from the experimental samples (Ulian and Valdrè, 2019). However, for a proper comparison between theoretical and experimental data, and to extend the knowledge on the mineral component of bony tissues, it is necessary to consider in the DFT simulations both type A and type B substitutions.

The present paper aims at filling this gap. For computational reasons, the focus is on a completely carbonated type-AB apatite structure, and the type-B defect was included in the cited CAp model, using sodium as counter-balancing ion (M^+ in the type-B formation reaction). The specific position of the Na^+ ion was chosen according to previous DFT characterization of both type-B and type-AB carbonated (hydroxyl)apatite models (Ulian et al., 2014), namely, sodium substitutes one of the calcium ions in the hexagonal channel (see ***Figure 1***). The structural model here employed to calculate the thermodynamic and thermoelastic properties is not a solid solution and refers to a specific symmetry-independent configuration with Na6/Ca6 substitution, which is the most stable from an energetic point of view (Ulian et al., 2014).

In the present simulations, the choice of sodium as counter-ion is explained and justified by several works during the last two decades that report:

(i) the presence of this cation in both natural (bone tissues) and synthetic apatite minerals (Dorozhkin, 2009; Dorozhkin, 2011),

(ii) the crystal-chemistry and structural properties of Na-bearing carbonated apatite (Fleet and Liu, 2004; Fleet and Liu, 2007) and

(iii) the infrared and Raman spectroscopic features of this mineral phase (Fleet et al., 2004; Khan et al., 2013; Yoder et al., 2019).

The elastic properties of this model were then evaluated both in static conditions (0 K) and at different pressure and temperature settings by means of the quasi-harmonic approximation framework. At the same time, specific thermodynamic properties, such as the coefficient of volumetric thermal expansion and the heat capacity) were calculated at selected *P*-*T* settings. Finally, all the obtained results were compared and discussed against previous experimental and theoretical data reported in literature, when available.

COMPUTATIONAL METHODS

The present quantum-mechanical analysis was conducted by means of the *ab initio* CRYSTAL17 code (Dovesi et al., 2018), employing the density functional theory (DFT).

Within this framework, the hybrid functional B3LYP (Lee et al., 1988; Becke, 1993) was selected because of its well-known capabilities for the structural, vibrational, thermodynamics, and elastic characterization of crystalline solids (Valenzano et al., 2006; Demichelis et al., 2010; Dovesi et al., 2011; Erba et al., 2014; Belmonte, 2017), and also apatite minerals (Corno et al., 2006; Peccati et al., 2014; Ulian et al., 2014; Ulian and Valdrè, 2018b; Ulian and Valdrè, 2018a; Ulian and Valdrè, 2019). As done in a recent work on type-A carbonated apatite (Ulian and Valdrè, 2019), the DFT-D2 correction proposed by Grimme (2006), and adapted for the B3LYP functional (Civalleri et al., 2008), was included provide adequate accounting of dispersive forces (B3LYP-D* approach).

The all-electron Gaussian-type orbital basis sets adopted in the present work were the same used in previous studies on hydroxylapatite and carbonated (hydroxyl)apatite (Ulian et al., 2014; Ulian et al., 2016; Ulian et al., 2018). More into details, calcium, sodium, phosphorous, oxygen and carbon atoms were described by means of 86-511G(2d) (Valenzano et al., 2007), 8-511G (Dovesi et al.,

1991), 85-21G(d) (Corno et al., 2006), 6-31G* (Corno et al., 2006) and 6-21G* (Catti et al., 1993), respectively.

The exchange-correlation contribution was evaluated by numerical integration of the electron density and its gradient over the volume of the unit cell, using a pruned grid consisting of 75 points and 974 angular points. The tolerances for truncation of the Coulomb and exchange integrals were set to 10^{-8} and 10^{-16}, respectively, which means that, when the overlap between two atomic orbitals is lower than the imposed threshold, the corresponding integral is either discarded or treated with less precision, as explained by Dovesi et al. (2018). The diagonalization of the Hamiltonian matrix was conducted at 36 *k*-points in the reciprocal space using a 4 × 4 × 4 Monkhorst-Pack net (Monkhorst and Pack, 1976).

The geometry optimization of the lattice and the internal coordinates was conducted with an analytical gradient method for the atomic positions and a numerical gradient for the unit cell parameters (Dovesi et al., 2018). The convergence on the unit cell geometry was reached when the gradient and the maximum atomic displacement were lower than $1 \cdot 10^{-5}$ Ha bohr^{-1} and $4 \cdot 10^{-5}$ bohr, respectively, with respect to the previous optimization step.

Static (0 K) equation of state and the quasi-harmonic approximation (QHA, *vide infra*) analyses were performed by considering eleven unit cell volumes of type-AB CAp between $0.82 \cdot V_{eq}$ and $1.12 \cdot V_{eq}$, with V_{eq} being the equilibrium volume of the mineral obtained after geometry optimization of the lattice parameters and atomic positions. Each unit cell was fully optimized at constant volume, obtaining an energy vs volume, $E(V)$, curve that was analysed in terms of a phenomenological, volume-integrated third-order Birch-Murnaghan (BM3) equation of state, as formulated by Hebbache and Zemzemi (2004):

$$E = E_0 + \frac{9}{16} K_0 V_0 \{K'(\eta^2 - 1)^3 + [(\eta^2 - 1)^2 (6 - 4\eta^2)]\} \quad (1)$$

where $\eta = (V/V_0)^{-1/3}$, K_0 is the bulk modulus, $K' = \partial K_0 / \partial P$ and V_0 the volume at zero pressure (and E_0 the corresponding unit cell energy). Using the equation of state parameters found in Eq.(1) it

is possible to calculate the pressure state, *P*, of the system by using the well-known BM3 formulation (Birch, 1947):

$$P = \frac{3}{2}K_0\left[\eta^{-7/3} - \eta^{-5/3}\right]\left\{1 - \frac{3}{4}(4 - K')\left(\eta^{-2/3} - 1\right)\right\} + P_0 \quad (2)$$

with P_0 the reference pressure.

The quasi-harmonic approximation was employed as a suitable framework to include the thermal effects on the elastic properties and to derive important thermodynamic parameters of type-AB carbonated apatite. The interested reader can find details on this approach in literature focused on the theory behind QHA (see, for instance Anderson, 1995; Erba, 2014; Ulian et al., 2020), as only the relevant approaches are here briefly summarized. The dependence of phonon properties of the mineral on the unit cell volume was included by interpolating the Helmholtz free energy in terms of the above cited equation of state formulation, finding the minimum volume and the bulk modulus at different *P*-*T* settings as described by Belmonte (2017). Other quasi-harmonic thermodynamic properties were obtained from polynomial interpolation of the harmonic ones at each calculated *V*(*P*,*T*) and their relationships. The QHA analysis was performed, starting from the quantum-mechanical results, by means of the Quantas package, a specifically written software for the analysis of minerals and synthetic solid phases (Ulian and Valdrè, 2020a).

Phonon properties were calculated at Γ-point (Pascale et al., 2004; Tosoni et al., 2005). While the size of the unit cell of type-AB carbonated apatite (43 atoms) is sufficiently large for an accurate description of the thermoelastic and thermodynamic properties obtained from the optical contributions (Prencipe et al., 2011; Ulian and Valdrè, 2019), the lack of phonon dispersion relations can not provide the thermodynamics arising from the acoustic branch. To improve the overall quality of the data, particularly at low temperatures, we considered the approach proposed by Kieffer (1979), which was discussed and adopted in recent literature within the quasi-harmonic approximation framework (Belmonte et al., 2016; De La Pierre and Belmonte, 2016). However, since no elastic

This is the peer-reviewed, final accepted version for American Mineralogist, published by the Mineralogical Society of America.
The published version is subject to change. Cite as Authors (Year) Title. American Mineralogist, in press.
DOI: https://doi.org/10.2138/am-2021-7826. http://www.minsocam.org/

moduli have been calculated in the present work, we assumed the shear modulus μ, necessary to calculate the seismic wave velocity (and then the acoustic modes), as $\mu \cong 3/5\,K$.

Furthermore, the infrared spectra at each unit cell volume were analytically calculated by means of a Coupled-Perturbed Kohn-Sham approach, as described by Ferrero and co-workers (Ferrero et al., 2008a; Ferrero et al., 2008b; Ferrero et al., 2008c; Ferrero et al., 2008d). To complete the overall vibrational picture, the Raman intensities and related spectrum were also obtained using the Placzek approximation (Placzek, 1934), where the key properties involved in computing non-resonant Raman susceptibilities are the partial derivatives of the polarizability tensor with respect to atomic positions, as described by Maschio and collaborators (Maschio et al., 2013a; Maschio et al., 2013b).

RESULTS AND DISCUSSION

Unit cell compression at 0 K

The simulation results (lattice parameters, bond and interaction lengths and PO_4 tetrahedral volumes) related to the compression and expansion of the unit cell of type-AB carbonated apatite in static conditions are reported in **Table 1**. The table reports also the pressure state at each unit cell volume, as calculated with Eq.(2) using the parameters of the volume-integrated Birch-Murnaghan equation of state, which were K_0 = 104.3(8) GPa, K' = 4.3(1) and V_0 = 517.9(2) Å^3. A graphical representation of some of the most relevant results are reported also in ***Figure 2*** as a function of pressure.

While the constant-volume geometry optimizations were performed without any symmetry constrain, *i.e.* using space group *P*1, the calculated lattice parameters closely resemble those of an hexagonal unit cell. At equilibrium (0 GPa), these parameters showed a very small difference with those experimentally measured by Fleet and Liu (2007) for a similar Na-bearing type-AB carbonated apatite of synthetic nature (Δa = –0.0497 Å, Δb = –0.0929 Å and Δc = –0.0397 Å). According to the theoretical investigation on the carbonate ion mobility in the hexagonal calcium channel reported by Peccati and co-workers (2014), the type-A substitution of carbonate ion is almost free to rotate at zero

compression, which explains the experimental $P\bar{3}$ symmetry of the type-A carbonated hydroxylapatite (Fleet and Liu, 2003). However, in literature it was not found any report of the effects of the type-B CO_3^{2-} ion position on the mineral structures, either alone or in combination with type-A substitutions, which would enhance the comparison of the present data with the experimental ones.

Making a comparison to previous simulations at the DFT/B3LYP level of theory of Ulian et al. (2014), the present results show that including dispersive effects is a real improvement for DFT simulations on carbonated apatite minerals. Unit cell volume is smaller due to the inclusion of the dispersive forces in the total energy calculation. In fact, even though GGA-based functionals (including hybrid ones as B3LYP) overestimate static volumes (*i.e.* unit cell volumes at absolute zero without zero-point correction), the B3LYP-D* approach provides smaller volumes ($\Delta V \approx -8$ Å^3). Then, by including also zero-point and thermal effects, it results $V^0_{B3LYP-D*}(298.15\ K, 0\ GPa) \cong V^0_{experimental}(298.15\ K, 0\ GPa) < V^0_{B3LYP}(298.15\ K, 0\ GPa)$. This explains also the importance of defining zero-point and thermal effects, besides static effects, on computed volumes.

The variation of the unit cell volume lattice parameters with pressure is non-linear, as well as the mean bond lengths, in line with the experimental findings of Liu and co-workers (2011). Some subtle variations are reported for the long-range interactions involving the cations (Ca^{2+}, Na^+) and the neighbouring oxygens, either from PO_4^{3-} and CO_3^{2-} groups. No sign of high-pressure transitions was evinced from the simulation results, albeit a small decrease of the *c* lattice parameter at –9.3 GPa suggests a possible instability of the structure. Since lattice expansion typically occurs during heating, this result could be indirectly related to the thermal decomposition of the mineral studied with combined thermal analysis and Fourier transform infrared (FTIR) spectroscopy (Barinov et al., 2006). The static third-order Birch-Murnaghan parameters are in line with those experimentally obtained by Liu and co-workers (2011) for the synthetic LM006 sample, K_0 = 89(2) GPa, K' = 4.1(6) and V_0 = 529.17(9) Å^3. At the experimental level, it was also found that carbonated apatite has lower stiffness than stoichiometric hydroxylapatite, whose bulk modulus was calculated as K_0 = 97.5 GPa (Brunet

et al., 1999). This means a reduction of the bulk modulus of about –10% for the LM006 sample. Considering the recently reported theoretical K_0 = 115.5(1) of OHAp at 0 K (Ulian and Valdrè, 2018b), in the present work the type-AB CAp showed a bulk modulus value lowered by about –10%, again in better agreement with the experimental LM006 data of Liu et al. (2011).

It is important stressing that in the present work the stoichiometry of the simulated model is $Ca_9Na(PO_4)_5(CO_3)^B(CO_3)^A$, corresponding to a carbonate and sodium contents of 15.0 wt.% and 2.9 wt.%, respectively. Instead, the chemical composition of the experimental LM006 sample reported by Liu and co-workers (2011) was $Ca_{9.66}Na_{0.35}(PO_4)_{5.56}(CO_3)_{0.44}(OH)_{1.45}(CO_3)_{0.33}$, meaning that it was a type-AB carbonated hydroxylapatite with 5.8 wt.% of CO_3^{2-} and 1.0 wt.% of Na^+. The differences between our theoretical data and the experimental results could be due, other than the different temperature of acquisition (0 K *vs* 298.15 K, respectively), to the presence of hydroxyl groups in the synthetic specimen and the lower carbonate content. Also, the experimental samples were in powder form, whereas our data refers to an ideal single-crystal type-AB carbonated apatite. Hence, the different crystal-chemistry of the theoretical model and of the specimen could have some influence on the elastic properties of the mineral. Unfortunately, there are not at present any other experimental data on type-AB carbonated apatite that can be used as comparison basis.

Considering the axial compressibilities using a linearized third-order Birch-Murnaghan formulation, the fitting procedure yielded a_0 = 9.339(8) Å, $M_0(a)$ = 229(17) GPa, $M'(a)$ = 25(3) for the **a**-axis, b_0 = 9.292(7) Å, $M_0(b)$ = 282(15) GPa, $M'(b)$ = 12(2) for the **b**-axis and c_0 = 6.875(3) Å, $M_0(c)$ = 463(21) GPa, $M'(c)$ = 14(2) for the **c**-axis. Thus, the behaviour is anisotropic, with the ratio $M_0(a) : M_0(b) : M_0(c)$ equal to 1 : 1.23 : 2.02. Compared to simulated stoichiometric hydroxylapatite (Ulian and Valdrè, 2018b), whose axial moduli and their first derivatives were $M_0(a)$ = 300(15) GPa, $M'(a)$ = 13(4) and $M_0(c)$ = 514(26) GPa, $M'(c)$ = 9(6), the carbonate ion substitutions led to a softer mineral phase, in particular along the **a** lattice vector where both type-A and type-B CO_3^{2-} ions are aligned. In addition, the type-B carbonate defect further lowered the axial moduli if compared to type-A CAp (Ulian and Valdrè, 2019). It is necessary to stress again that these results are dependent on

the crystallographic site occupied by the carbonate ion. Indeed, there are six phosphate ions in the unit cell that could be substituted by a carbonate ion, leading to at least six different type-A – type-B CO_3^{2-} configurations, which in turn could provide different elastic behaviours of the mineral. This kind of analysis is beyond the scope of the present paper, but will be the subject of further investigations in the future.

Vibrational spectroscopy

This section is devoted to a detailed analysis of the effects of compression on the vibrational features of type-AB carbonated apatite, whose unit cell is associated with $43 \times 3 - 3 = 126$ normal (optic) modes with vibrational character. A brief review of the fundamental vibrational transitions occurring in apatite-based minerals is necessary and is reported in the following.

Several authors already discussed the irreducible representations (IRREP) of the "free" phosphate group, which gives four vibrational modes (see, for instance, Tsuda and Arends, 1994; Rehman and Bonfield, 1997; Cuscó et al., 1998): the symmetric P–O stretching (labelled as ν_1, IRREP A_1, 938 cm^{-1}; the symmetric O–P–O bending ($\nu 2$, E, 420 cm^{-1}); the asymmetric P–O stretching (ν_3, F, 1017 cm^{-1}) and the asymmetric O–P–O bending (ν_4, F, 567 cm^{-1}). When the PO_4 tetrahedron deviates from ideality, as in the case of carbonated apatite, it may give up to nine vibrational signals due to the degeneracy of the high-symmetry modes (two peaks from E and three from F). The same applies to the carbonate ion that, ideally, presents only four modes: in-plane O–C–O bending (ν_4, E'), out-of-plane O–C–O bending (ν_2, A''), symmetric C–O stretching (ν_1, A_1') and asymmetric C–O stretching (ν_3, E'). In apatite, the ν_3 and ν_4 modes are not degenerate anymore and give origin to two doublets (Ulian et al., 2013b). It is worth remembering that the some of the vibrational modes (*e.g.* the symmetric P–O and C–O stretchings) are active in apatite minerals, although they have very small intensities due to the small variation of the dipole moment of the mineral and are usually not evident in the experimental spectra (Ulian et al., 2013b; Ulian et al., 2014).

This is the peer-reviewed, final accepted version for American Mineralogist, published by the Mineralogical Society of America.
The published version is subject to change. Cite as Authors (Year) Title. American Mineralogist, in press.
DOI: https://doi.org/10.2138/am-2021-7826. http://www.minsocam.org/

Figure 3 reports the calculated infrared spectra of type-AB CAp in the range 500 cm^{-1}–1900 cm^{-1} at equilibrium and at different pressures (unit cell volumes). The calculated vibrational modes at 0 GPa are in good agreement with previous simulations on the same structure by Ulian et al. (2014), with the slightly shifted peaks due to the inclusion in our work of the dispersive forces correction. Also, while the overall appearance of the spectra is similar, some differences can be noted due to the employed method to calculate the infrared intensities. In fact, in the previous work of Ulian and co-workers (2014) they were calculated via Berry phase approach and the peaks were described using pure Lorentzian functions, whereas in our work the IR intensities were analytically evaluated using a coupled perturbed Kohn-Sham approach and the spectra were calculated using a classical absorption formula. However, for details on the peak assignments to specific normal modes, the reader is encouraged to refer to the cited paper (Ulian et al., 2014) because here, for the sake of brevity, they are only graphically reported in ***Figure 3a***. The DFT framework here considered provided results in very good agreement with the recent FTIR analysis of synthetic mixed type-AB carbonated hydroxylapatite samples (Pham Minh et al., 2014). In particular, considering carbonate ion vibrational modes, they were experimentally measured as ν_2(type-B) = 870 cm^{-1}, ν_2(type-A) = 880 cm^{-1}, ν_3(type-B) = 1415 and 1450 cm^{-1} and ν_3(type-A) = 1545 cm^{-1}, whereas the theoretical data showed ν_2(type-B) = 875 cm^{-1} ν_2(type-A) = 887 cm^{-1}, ν_3(type-B) = 1476 cm^{-1} and 1548 cm^{-1} and ν_3(type-A) = 1445 cm^{-1} and 1598 cm^{-1}. The slight deviation related to the asymmetric C–O stretching mode could be related to the computational approach, as also explained in the work of Ulian and co-workers (2014).

When type-AB CAp is subject to compression, striking variations can be observed in the positions of the different peaks. In general, all the modes are blue shifted by increasing pressure, except for the ν_4 CO_3^{2-} band that is red shifted, a result that is in accordance with both experimental and theoretical evidences related to uniaxial and biaxial strains in hydroxylapatite investigated with Raman spectroscopy (Pezzotti et al., 2015; Ulian and Valdrè, 2018a). Pressure affects the vibrational modes with different intensity, *i.e.* how much each peak is shifted in the spectrum, in some cases resulting in convolution or deconvolution of the signals. Also, the results suggest that unit cell expansion did

This is the peer-reviewed, final accepted version for American Mineralogist, published by the Mineralogical Society of America.
The published version is subject to change. Cite as Authors (Year) Title. American Mineralogist, in press.
DOI: https://doi.org/10.2138/am-2021-7826. http://www.minsocam.org/

not sensibly affect the overall infrared spectrum when the pressure is higher than about -1.3 GPa. Both the CO_3^{2-} and $PO4^{3-}$ asymmetric stretching modes (ν_3) are the most affected by the increased pressure, as they were shifted up to about 110 cm^{-1} at 33 GPa.

For the sake of completeness, the simulated Raman spectra of type-AB carbonated apatite are reported in ***Figure 4***. The intensity of the Raman peaks was calculated with the approach described in the Methods section, presenting an improvement with respect to the previous works of Ulian and co-workers (Ulian et al., 2013b; Ulian et al., 2014), where only the vibrational frequency of the Raman signals were obtained. In the Raman case, complementarily with the infrared spectroscopy, the most intense phosphate and carbonate peaks are associated to the symmetric stretching modes $\nu_1(PO_4)$ and $\nu_1(CO_3)$, respectively.

In **Table 2**, the calculated vibrational frequencies of both type A and type B carbonate ion are reported, as they are commonly used to identify the type of carbonated hydroxylapatite. It is possible to note that both ν_2 normal modes are associated to negative mode-gamma Grüneisen parameters, *i.e.* $\gamma_i = \partial \ln \nu_i / \partial \ln V < 0$. Usually, this could be a sign of phonon instability of the mineral phase, related also to mechanical instability of the structure, especially when the frequency value of the mode becomes negative (imaginary frequency). However, the rate of frequency shift related to increasing pressure (decreasing volume) is very small, hence the type-AB carbonated apatite model is stable in the pressure range explored in the present work.

Thermoelastic and thermodynamic properties

The present theoretical investigation of the thermodynamic and thermoelastic properties was performed within the quasi-harmonic approximation between 0 GPa and 32 GPa (with step of 1 GPa). The upper limit of this characterization was chosen according to the minimum unit cell volume investigated in static conditions (*vide supra*), in order to avoid extrapolating the results. However, the choice of the temperature range for the determination of the above cited properties is not a trivial task. According to recent differential thermogravimetric (DTG) analyses on synthesized bone-like

This is the peer-reviewed, final accepted version for American Mineralogist, published by the Mineralogical Society of America.
The published version is subject to change. Cite as Authors (Year) Title. American Mineralogist, in press.
DOI: https://doi.org/10.2138/am-2021-7826. http://www.minsocam.org/

carbonated apatite without sodium cations, there are several steps of thermal decomposition of this mineral, mainly due to carbonate ion loss as carbon dioxide as reported by Pham Minh and co-workers (2014). More into details, type-AB carbonated apatite thermally decomposes between ca. 940 K and 1520 K, with two small peaks in the DTG curve related to the loss of type-A CO_3^{2-} in the range 940 – 1140 K and a strong, broad peak in between 1270 K and 1520 K due to type-B carbonate ion decomposition. As we previously explained (Ulian and Valdrè, 2019), the QHA method is not able to directly describe chemical reactions, such as thermal decomposition, because it calculates the response of a system upon small perturbations (on volume and/or temperature). For this reason, the thermodynamic and thermoelastic properties of the present type-AB CAp model were evaluated between 0 and 800 K (with step of 10 K), hence below the occurrence of the structural thermal decomposition of the mineral.

As introduced in the Computational Method section, the quasi-harmonic analysis was conducted using the Quantas code (Ulian and Valdrè, 2020a), employing an equation of state fitting scheme to simultaneously obtain the minimum volume, the bulk modulus K_T and its first derivative K' at each P-T condition. The selected equation of state (EoS) formulation was the volume-integrated third-order Birch-Murnaghan described in Eq.(2).

Unit cell volume, coefficient of volumetric thermal expansion, α_V, isothermal (K_T) and adiabatic (K_S) bulk moduli and first derivative of isothermal bulk modulus K' in the temperature range 0 – 800 K are reported in ***Figure 5***, whereas contour plots of the same properties at different P-T conditions are presented in ***Figure 6***.

More into details, the unit cell volume (***Figure 5a***) and the coefficient of thermal expansion (***Figure 5b***) increase with temperature and drastically shrink with pressure. In agreement with previous investigations on type-A CAp (Ulian and Valdrè, 2019), no negative $\alpha_V(T,P)$ was calculated in the low-temperature regime (about 0 – 100 K) as instead reported for stoichiometric hydroxylapatite (Ulian and Valdrè, 2018b), further confirming that the hydroxyl groups are responsible for this behaviour. In addition, $V(T)$ data at 0 GPa were fitted considering the second-order polynomial

This is the peer-reviewed, final accepted version for American Mineralogist, published by the Mineralogical Society of America.
The published version is subject to change. Cite as Authors (Year) Title. American Mineralogist, in press.
DOI: https://doi.org/10.2138/am-2021-7826. http://www.minsocam.org/

function normalized to 293 K, proposed by Brunet et al. (1999) in their investigation of the thermal properties of apatite minerals. The adopted expression is the following one:

$$\frac{V(T)}{V(293)} = 1 + \alpha_1(T - 293) + \alpha_2(T - 293)^2 \quad (3)$$

and resulted in $\alpha_1 = 2.67 \cdot 10^{-5}$ K^{-1} and $\alpha_2 = 7.55 \cdot 10^{-9}$ K^{-2}. The calculated parameters of Eq.(3) are larger than those of both type-A carbonated apatite ($\alpha_1 = 2.56 \cdot 10^{-5}$ K^{-1} and $\alpha_2 = 5.73 \cdot 10^{-9}$ K^{-2}) and stoichiometric OHAp ($\alpha_1 = 2.57 \cdot 10^{-5}$ K^{-1} and $\alpha_2 = 7.52 \cdot 10^{-9}$ K^{-2}) (Ulian and Valdrè, 2018b; Ulian and Valdrè, 2019), showing the subtle interplay between type-A and type-B CO_3^{2-} in determining the overall thermal expansion of the mineral. In fact, while it was suggested that the unit-cell volume expansion was lower in type-A CAp than in hydroxylapatite because of the increased O_{CO3} --- Ca^{2+} interactions (Ulian and Valdrè, 2020b), the type-B carbonate group (planar) has less interactions with the neighbouring cations than the substituted PO_4^{3-} ion (tetrahedral group). Of course, in mixed type-AB carbonated apatite there is a competing effect between type-B and type-A CO_3^{2-} on the thermal expansion coefficient, which explains the slightly higher α_1 and α_2 parameters with respect to stoichiometric OHAp.

While structural data of type-AB carbonated apatite at simultaneous *P-T* variation are not yet available in both experimental and theoretical literature, it is possible to compare the pressure evolution of the unit cell volume at 300 K with the results of Liu and co-workers (2011). ***Figure 7*** reports the calculated absolute lattice volume, which is in very good agreement with the experimental data, as the blue line falls between the two datasets. This is an important proof of the quality of the present theoretical data, as the quasi-harmonic approximation framework here employed provided an adequate description of type-AB carbonated apatite.

The mineral stiffness reduced with increasing temperature, while increasing pressure augmented the bulk modulus. At 0 GPa and 300 K, the calculated BM3 parameters were K_T = 101.3 GPa, K' = 4.13 and V_0 = 525.053 GPa. Compared to the theoretical value of hydroxylapatite calculated with the

same computational approach and at the same *P-T* settings (K_T = 109.65 GPa), the contemporary presence of both types of carbonate substitutions led to a reduction of the bulk modulus of about ΔK_T = -7.6%. This observation shows also that increasing the carbonate content from type-A to type-AB further reduced the bulk modulus, as for type-A ΔK_T was calculated as about -6.1% (Ulian and Valdrè, 2020b). The variation of bulk modulus with carbonate ion concentration is also in line with the experimental findings of Liu and co-workers (2011), who assessed a ΔK_T value of about 10% and 15% for their analyses.

Figure 8 reports the entropy (***Figure 8a***) and the isobaric heat capacity (***Figure 8c***), which were plotted as a function of temperature at different pressures between 0 GPa and 30 GPa. It is worth stressing that the entropy term lacks the so-called anharmonic term, as described by Belmonte et al. (2016). In addition, these quantities were also reported as bidimensional contour at different *P-T* settings (***Figures 8b,d***). To the authors' knowledge, no experimental and theoretical data are available in literature for a direct comparison and full assessment of the results. However, both thermodynamic quantities increase with temperature and decrease with pressure, trends indicating a correct description of the physics of the mineral system.

For the sake of completeness, a summary of the most relevant thermodynamic and thermoelastic results of type-AB CAp calculated within the quasi-harmonic approximation are reported in **Table 3** (constant pressure P = 0 GPa) and in **Table 4** (constant temperature T = 300 K). These data could be a useful reference for future experimental and theoretical studies involving this complex mineral phase.

IMPLICATIONS

The present work was focused on a completely carbonated apatite structure presenting both type-A CO_3^{2-}/OH^- and type-B CO_3^{2-}/PO_4^{3-} substitutions (mixed type-AB), whose thermodynamic and thermoelastic properties were extensively investigated from a theoretical perspective.

Carbonated hydroxylapatite, containing a mixture of both type-A and type-B carbonate ions, is the main mineral phase in bone and dental tissues. According to previous analyses, dentin and cortical bone are made of about 73 wt.% of biological apatite, whereas up to about 95 wt.% is present in enamel, with a variable CO_3^{2-} content depending on the bony tissue (Elliott, 2002; Dorozhkin, 2009). In this context, modelling the anisotropic elastic properties of the mineral phase as a function of both crystal-chemical variations and *P*-*T* conditions is fundamental to both understand bone physiology and devise/develop better biomaterials for prosthetics and fillers.

Notwithstanding the crystal-chemistry of the employed mineral model here investigated in the context of geological/biological apatites presents no hydroxyl groups in the structure, and any other cationic/anionic substitution that typically occurs in experimental samples were not considered, this study clearly depicted the important role of both carbonate ion types in determining the elastic and thermodynamic properties. Indeed, only by decoupling (and eventually re-coupling) the effects of single substitutions it is possible to understand variations on structural, elastic and thermodynamic properties of mineral phases as complex as biological apatite or other phases. For example, it was shown that the temperature-dependent unit cell expansion in type-AB is due to the combination of both A- and B-substitutions, with the latter being predominant in the observed result. Considering also previous quantum-mechanical modelling of hydroxylapatite (Ulian and Valdrè, 2018b) and type-A carbonated apatite (Ulian and Valdrè, 2019), the introduction of type-A and type-B carbonate defects deeply affects the elastic properties, causing the reduction of the bulk modulus of the mineral phase. In general, the results at ambient temperature were in line with the few ones available in literature (Liu et al., 2011), providing more insights at the atomic scale and extending the knowledge to wide pressure and temperature ranges.

For the first time to the author's knowledge, a complete characterization of the vibrational properties of type-AB carbonated apatite under the effect of hydrostatic compression/expansion was reported, which could be very useful for experimentalists in calibrating infrared/Raman techniques for the determination of the pressure state of the mineral.

In future, simulations of larger models (*e.g.* using supercells) that can accommodate for different anionic/cationic substitutions and, generally, with chemical composition of the mineral closer to the experimental ones could be performed to investigate thermodynamics and the elastic behaviour of carbonated (hydroxyl)apatite for specific applications. To cite some of them, it could be possible to realize either a biomimetic material for fillers and prosthetics in the context of biomaterial applications or an agglomerate for raw materials, waste disposal and/or geopolymer applications. Depending on the use, it is necessary to tune the bulk and surface properties of the carbonated hydroxylapatite mineral, which in turn depend on the amount (and crystallographic site occupancies) of the type-A and type-B carbonate ions and other substituent.

In this framework, suitable quantum-mechanical simulations at the Density Functional Theory level represent an invaluable tool to pre-determine the thermodynamic and elastic properties of solid phases, helping the experimental researches.

Acknowledgements

The present work was supported by the Regione Emilia Romagna project No. PA2019-11452/RER.

References

Albee, F.H. (1920) Studies in bone growth – triple calcium phosphate as stimulus to osteogenesis. Annals of Surgery, 71, 32-39.

Anderson, O.L. (1995) Equation of state of solids for geophysics and ceramic science. 405 p. Oxford University Press, New York, US.

Astala, R., and Stott, M.J. (2005) First principles investigation of mineral component of bone: CO3 substitutions in hydroxyapatite. Chemistry of Materials, 17(16), 4125-4133.

Barinov, S.M., Rau, J.V., Cesaro, S.N., Ďurišin, J., Fadeeva, I.V., Ferro, D., Medvecky, L., and Trionfetti, G. (2006) Carbonate release from carbonated hydroxyapatite in the wide temperature rage. Journal of Materials Science: Materials in Medicine, 17(7), 597-604.

Becke, A.D. (1993) Density-Functional Thermochemistry .3. The Role of Exact Exchange. Journal of Chemical Physics, 98(7), 5648-5652.

Belmonte, D. (2017) First Principles Thermodynamics of Minerals at HP-HT Conditions: MgO as a Prototypical Material. Minerals, 7(10), 183.

Belmonte, D., Gatti, C., Ottonello, G., Richet, P., and Zuccolini, M.V. (2016) Ab Initio Thermodynamic and Thermophysical Properties of Sodium Metasilicate, Na2SiO3, and Their Electron-Density and Electron-Pair-Density Counterparts. Journal of Physical Chemistry A, 120(44), 8881-8895.

Birch, F. (1947) Finite elastic strain of cubic crystal. Physical Review, 71, 809-824.

Brunet, F., Allan, D.R., Redfern, S.A.T., Angel, R.J., Miletich, R., Reichmann, H.J., Sergent, J., and Hanfland, M. (1999) Compressibility and thermal expansivity of synthetic apatites, Ca-5(PO4)(3)X with X = OH, F and Cl. European Journal of Mineralogy, 11(6), 1023-1035.

Catti, M., Pavese, A., Dovesi, R., and Saunders, V.R. (1993) Static lattice and electron properties of MgCO3 (Magnesite) calculated by ab-initio periodic Hartree-Fock methods. Physical Review B, 47, 9189-9198.

Civalleri, B., Zicovich-Wilson, C.M., Valenzano, L., and Ugliengo, P. (2008) B3LYP augmented with an empirical dispersion term (B3LYP-D*) as applied to molecular crystals. CrystEngComm, 10(4), 405-410.

Corno, M., Busco, C., Civalleri, B., and Ugliengo, P. (2006) Periodic ab initio study of structural and vibrational features of hexagonal hydroxyapatite Ca10(PO4)6(OH)2. Physical Chemistry Chemical Physics, 8, 2464-2472.

Cuscó, R., Guitian, F., de Aza, S., and Artus, L. (1998) Differentiation between hydroxyapatite and beta-tricalcium phosphate by means of mu-raman spectroscopy. Journal of the European Ceramic Society, 18(9), 1301-1305.

De La Pierre, M., and Belmonte, D. (2016) Ab initio investigation of majorite and pyrope garnets: Lattice dynamics and vibrational spectra. American Mineralogist, 101(1), 162-174.

Demichelis, R., Civalleri, B., Ferrabone, M., and Dovesi, R. (2010) On the Performance of Eleven DFT Functionals in the Description of the Vibrational Properties of Aluminosilicates. International Journal of Quantum Chemistry, 110(2), 406-415.

Dorozhkin, S.V. (2009) Calcium Orthophosphates in Nature, Biology and Medicine. Materials, 2, 399-498.

-. (2010) Nanosized and nanocrystalline calcium orthophosphates. Acta Biomaterialia, 6(3), 715-734.

-. (2011) Calcium orthophosphates: occurrence, properties, biomineralization, pathological calcification and biomimetic applications. Biomatter, 1(2), 121-164.

Dovesi, R., De La Pierre, M., Ferrari, A.M., Pascale, F., Maschio, L., and Zicovich-Wilson, C.M. (2011) The IR vibrational properties of six members of the garnet family: A quantum mechanical ab initio study. American Mineralogist, 96(11-12), 1787-1798.

Dovesi, R., Erba, A., Orlando, R., Zicovich-Wilson, C.M., Civalleri, B., Maschio, L., Rerat, M., Casassa, S., Baima, J., Salustro, S., and Kirtman, B. (2018) Quantum-mechanical condensed matter simulations with CRYSTAL. Wiley Interdisciplinary Reviews-Computational Molecular Science, 8(4), E1360.

Dovesi, R., Roetti, C., Freyria Fava, C., Prencipe, M., and Saunders, V.R. (1991) On the elastic properties of lithium, sodium an potassium oxide. An ab initio study. Chemical Physics, 156, 11-19.

Elliott, J.C. (2002) Calcium phosphate biominerals. Reviews in Mineralogy and Geochemistry, 48.

Erba, A. (2014) On combining temperature and pressure effects on structural properties of crystals with standard ab initio techniques. Journal of Chemical Physics, 141(12), 124115.

Erba, A., Mahmoud, A., Belmonte, D., and Dovesi, R. (2014) High pressure elastic properties of minerals from ab initio simulations: The case of pyrope, grossular and andradite silicate garnets. Journal of Chemical Physics, 140(12), 124703.

Ferrero, M., Rerat, M., Kirtman, B., and Dovesi, R. (2008a) Calculation of first and second static hyperpolarizabilities of one- to three-dimensional periodic compounds. Implementation in the CRYSTAL code. Journal of Chemical Physics, 129(24), 244110.

Ferrero, M., Rerat, M., Orlando, R., and Dovesi, R. (2008b) The calculation of static polarizabilities of 1-3D periodic compounds. The implementation in the CRYSTAL code. Journal of Computational Chemistry, 29(9), 1450-1459.

-. (2008c) Coupled perturbed Hartree-Fock for periodic systems: The role of symmetry and related computational aspects. Journal of Chemical Physics, 128(1).

Ferrero, M., Rerat, M., Orlando, R., Dovesi, R., and Bush, I.J. (2008d) Coupled perturbed Kohn-Sham calculation of static polarizabilities of periodic compounds - art. no. 012016. Ab Initio Simulation of Crystalline Solids: History and Prospects - Contributions in Honor of Cesare Pisani, 117, 12016-12016.

Fleet, M.E. (2009) Infrared spectra of carbonate apatites: n2-Region bands. Biomaterials, 30, 1473-1481.

Fleet, M.E., and Liu, X. (2007) Coupled substitution of type A and B carbonate in sodium-bearing apatite. Biomaterials, 28(6), 916-926.

-. (2008) Type A-B carbonate chlorapatite synthesized at high pressure. Journal of Solid State Chemistry, 181(9), 2494-2500.

Fleet, M.E., and Liu, X.Y. (2003) Carbonate apatite type A synthesized at high pressure: new space group (P(3)over-bar) and orientation of channel carbonate ion. Journal of Solid State Chemistry, 174(2), 412-417.

-. (2004) Location of type B carbonate ion in type A-B carbonate apatite synthesized at high pressure. Journal of Solid State Chemistry, 177(9), 3174-3182.

Fleet, M.E., Liu, X.Y., and King, P.L. (2004) Accommodation of the carbonate ion in apatite: An FTIR and X-ray structure study of crystals synthesized at 2-4 GPa. American Mineralogist, 89(10), 1422-1432.

Fleet, M.E., Liu, X.Y., and Liu, X. (2011) Orientation of channel carbonate ions in apatite: Effect of pressure and composition. American Mineralogist, 96(7), 1148-1157.

Grimme, S. (2006) Semiempirical GGA-type density functional constructed with a long-range dispersion correction. Journal of Computational Chemistry, 27(15), 1787-1799.

Hebbache, M., and Zemzemi, M. (2004) Ab initio study of high-pressure behavior of a low compressibility metal and a hard material: Osmium and diamond. Physical Review B, 70(22).

Khan, A.F., Awais, M., Khan, A.S., Tabassum, S., Chaudhry, A.A., and Rehman, I.U. (2013) Raman spectroscopy of natural bone and synthetic apatites. Applied Spectroscopy Reviews, 48(4), 329-355.

Kieffer, S.W. (1979) Thermodynamics and lattice vibrations of minerals - 1. mineral heat capacities and their relationships to simple lattice vibrational models. Reviews of Geophysics and Space Physics, 17(1), 1-19.

Lee, C.T., Yang, W.T., and Parr, R.G. (1988) Development of the Colle-Salvetti Correlation-Energy Formula into a Functional of the Electron-Density. Physical Review B, 37(2), 785-789.

Liu, X., Shieh, S.R., Fleet, M.E., Zhang, L.F., and He, Q.A. (2011) Equation of state of carbonated hydroxylapatite at ambient temperature up to 10 GPa: Significance of carbonate. American Mineralogist, 96(1), 74-80.

Maschio, L., Kirtman, B., Rerat, M., Orlando, R., and Dovesi, R. (2013a) Ab initio analytical Raman intensities for periodic systems through a coupled perturbed Hartree-Fock/Kohn-Sham method in an atomic orbital basis. I. Theory. Journal of Chemical Physics, 139(16), 164101.

-. (2013b) Ab initio analytical Raman intensities for periodic systems through a coupled perturbed Hartree-Fock/Kohn-Sham method in an atomic orbital basis. II. Validation and comparison with experiments. Journal of Chemical Physics, 139(16), 164102.

Monkhorst, H.J., and Pack, J.D. (1976) Special points for Brillouin-zone integrations. Physical Review B, 8, 5188-5192.

Pascale, F., Zicovich-Wilson, C.M., Gejo, F.L., Civalleri, B., Orlando, R., and Dovesi, R. (2004) The calculation of the vibrational frequencies of crystalline compounds and its implementation in the CRYSTAL code. Journal of Computational Chemistry, 25(6), 888-897.

Peccati, F., Corno, M., Delle Piane, M., Ulian, G., Ugliengo, P., and Valdrè, G. (2014) CO_3^{2-} mobility in carbonate apatite as revealed by density functional modeling. Journal of Physical Chemistry C, 118(2), 1364-1369.

Peeters, A., DeMaeyer, E.A.P., VanAlsenoy, C., and Verbeeck, R.M.H. (1997) Solids modeled by ab initio crystal-field methods .12. Structure, orientation, and position of A-type carbonate in a hydroxyapatite lattice. Journal of Physical Chemistry B, 101(20), 3995-3998.

Peroos, S., Du, Z., and de Leeuw, N.H. (2006) A computer modelling study of the uptake, structure and distribution of carbonate defects in hydroxy-apatite. Biomaterials, 27, 2150-2161.

Pezzotti, G., Rondinella, A., Marin, E., Zhu, W., Aldini, N.N., Ulian, G., and Valdrè, G. (2017) Raman spectroscopic investigation on the molecular structure of apatite and collagen in osteoporotic cortical bone. Journal of the Mechanical Behavior of Biomedical Materials, 65, 264-273.

Pezzotti, G., Zhu, W.L., Boffelli, M., Adachi, T., Ichioka, H., Yamamoto, T., Marunaka, Y., and Kanamura, N. (2015) Vibrational algorithms for quantitative crystallographic analyses of hydroxyapatite-based biomaterials: I, theoretical foundations. Analytical and Bioanalytical Chemistry, 407(12), 3325-3342.

Pham Minh, D., Tran, N.D., Nzihou, A., and Sharrock, P. (2014) Novel one-step synthesis and characterization of bone-like carbonated apatite from calcium carbonate, calcium hydroxide and orthophosphoric acid as economical starting materials. Materials Research Bulletin, 51, 236-243.

Placzek, G. (1934) Handbuch der Radiologie. 208 p. Akademische Verlagsgeselschft, Leipzig.

Prencipe, M., Scanavino, I., Nestola, F., Merlini, M., Civalleri, B., Bruno, M., and Dovesi, R. (2011) High-pressure thermo-elastic properties of beryl (Al4Be6Si12O36) from ab initio calculations, and observations about the source of thermal expansion. Physics and Chemistry of Minerals, 38(3), 223-239.

Rabone, J.A.L., and de Leeuw, N.H. (2007) Potential routes to carbon inclusion in apatite materials: a DFT study. Physics and Chemistry of Minerals, 34, 495-506.

Rehman, I., and Bonfield, W. (1997) Characterization of hydroxyapatite and carbonated apatite by photo acoustic FTIR spectroscopy. Journal of Materials Science-Materials in Medicine, 8(1), 1-4.

Suda, H., Yashima, M., Kakihana, M., and Yoshimura, M. (1995) Monoclinic <--> Hexagonal Phase Transition in Hydroxyapatite Studied by X-ray Powder Diffraction and Differential Scanning Calorimeter Techniques. Journal of Physical Chemistry, 99(17), 6752-6754.

Tosoni, S., Pascale, F., Ugliengo, P., Orlando, R., Saunders, V.R., and Dovesi, R. (2005) Quantum mechanical calculation of the OH vibrational frequency in crystalline solids. Molecular Physics, 103(18), 2549-2558.

Tsuda, H., and Arends, J. (1994) Orientational micro-Raman spectroscopy on hydroxyapatite single crystals and human enamel crystallites. Journal of Dental Research, 73, 1703-1710.

Ulian, G., Moro, D., and Valdrè, G. (2016) First-principles study of structural and surface properties of (001) and (010) surfaces of hydroxylapatite and carbonated hydroxylapatite. Journal of Applied Crystallography, 49(6), 1893–1903.

-. (2018) Probing the interaction of (001) carbonated hydroxylapatite surfaces with water: a density functional investigation. Micro & Nano Letters, 13(1), 4-8.

-. (2020) Thermodynamic and thermoelastic properties of wurtzite-ZnS by Density Functional Theory. American Mineralogist, in press.

Ulian, G., and Valdrè, G. (2018a) Effect of mechanical stress on the Raman and Infrared bands of hydroxylapatite: a quantum mechanical first principle investigation. Journal of the Mechanical Behavior of Biomedical Materials, 77, 683-692.

-. (2018b) Equation of state of hexagonal hydroxylapatite (P6(3)) as obtained from density functional theory simulations. International Journal of Quantum Chemistry, 118(12), e25553.

-. (2019) First principle investigation of the thermomechanical properties of type A carbonated apatite. International Journal of Quantum Chemistry, 120, e26069.

-. (2020a) QUANTAS, a Python software for the analysis of solids from ab initio quantum mechanical simulations and experimental data. in preparation.

-. (2020b) Thermodynamic and thermoelastic data of georesources raw minerals: Zinc sulphide and apatite. Data in Brief, 29, 105265.

Ulian, G., Valdrè, G., Corno, M., and Ugliengo, P. (2013a) Periodic ab initio bulk investigation of hydroxylapatite and type A carbonated apatite with both pseudopotential and all-electron basis sets for calcium atoms. American Mineralogist, 98(2-3), 410-416.

Ulian, G., Valdrè, G., Corno, M., and Ugliengo, P. (2013b) The vibrational features of hydroxylapatite and type A carbonated apatite: a first principle contribution. American Mineralogist, 98(4), 752-759.

Ulian, G., Valdrè, G., Corno, M., and Ugliengo, P. (2014) DFT investigation of structural and vibrational properties of type B and mixed A-B carbonated hydroxylapatite. American Mineralogist, 99(1), 117-127.

Valenzano, L., Noel, Y., Orlando, R., Zicovich-Wilson, C.M., Ferrero, M., and Dovesi, R. (2007) Ab initio vibrational spectra and dielectric properties of carbonates: magnesite, calcite and dolomite. Theoretical Chemistry Accounts, 117(5-6), 991-1000.

Valenzano, L., Torres, F.J., Klaus, D., Pascale, F., Zicovich-Wilson, C.M., and Dovesi, R. (2006) Ab initio study of the vibrational spectrum and related properties of crystalline compounds; the

case of $CaCO_3$ calcite. Zeitschrift Fur Physikalische Chemie-International Journal of Research in Physical Chemistry & Chemical Physics, 220(7), 893-912.

Yoder, C.H., Bollmeyer, M.M., Stepien, K.R., and Dudrick, R.N. (2019) The effect of incorporated carbonate and sodium on the IR spectra of A- and AB-type carbonated apatites. American Mineralogist, 104(6), 869-877.

This is the peer-reviewed, final accepted version for American Mineralogist, published by the Mineralogical Society of America.
The published version is subject to change. Cite as Authors (Year) Title. American Mineralogist, in press.
DOI: https://doi.org/10.2138/am-2021-7826. http://www.minsocam.org/

Figure captions

Figure 1. Type-AB carbonated apatite model used in the present work, viewed from (a) [001] and (b) [010] directions. For the sake of clearness, four replicas of the unit cell are reported. Note that Na was included in the model according to previous works (Elliott, 2002; Fleet and Liu, 2007; Dorozhkin, 2009).

Figure 2. Structural variations of type AB carbonated apatite upon compression, in terms of (a-c) lattice parameters and (d-f) internal geometry (bond lengths). More into details, panel (a) reports the unit cell volume, (b) **a-** and **b-**axis lengths, (c) **c-**axis length, (d) P – O (e) type-A (C_A) and type-B (C_B) C – O bond lengths and (f) long-range interactions Ca --- O and Na --- O.

Figure 3. (a) Simulated infrared spectrum of type-AB carbonated apatite model at equilibrium. Relevant peaks are associated to the vibrational modes of specific ionic groups in the mineral (see text for details). (b) DFT/B3LYP-D* IR spectra of type-AB CAp at different pressure conditions. Specific spectral ranges related to the vibrational modes of different ionic groups in the structure are highlighted. Both images consider the IR spectroscopic range of 500 cm^{-1} – 1900 cm^{-1}.

Figure 4. (a) Raman spectrum of type-AB carbonated apatite, simulated at the DFT/B3LYP-D* level of theory. Specific normal modes are assigned to the related peaks in the spectrum. (b) Simulated Raman spectra of type-AB carbonated apatite between -9.3 GPa and 33.0 GPa. In both panels, the Raman spectroscopic range is 350 cm^{-1} – 1700 cm^{-1}.

Figure 5. Quasi-harmonic calculation of (a) unit cell volume, (b) coefficient of volumetric thermal expansion, α_V, (c) isothermal bulk modulus, K_T (solid lines) and adiabatic bulk modulus, K_S (dashed lines) and (d) first derivative of bulk modulus, *K'* calculated for type-AB carbonated apatite.

Figure 6. Bidimensional contour plots of (a) unit cell volume, (b) coefficient of volumetric thermal expansion, α_V, (c) adiabatic bulk modulus, K_S, and (d) first derivative of bulk modulus, *K'*, obtained from the quasi-harmonic approximation analysis on type AB CAp. Isolines of constant value for the different properties are reported as white lines in the plots.

Figure 7. Comparison between the pressure-induced unit cell volume variation of type AB carbonated apatite at 300 K calculated from DFT simulations (blue line) and the experimental results obtained from powder X-ray diffraction on carbonated apatite samples named LM006 (black circles) and LM005 (black squares) up to 10 GPa as reported by Liu et al. (2011).

Figure 8. Calculated thermodynamic quantities of type-AB carbonated apatite: (a) entropy, *S* as a function of temperature at different pressure states; (b) bidimensional contour plot of entropy at different *P-T* conditions; (c) isobaric heat capacity, C_P as a function of temperature at different pressure states; (d) bidimensional contour plot of C_P at different *P-T* conditions.

List of Tables

Table 1. Type-AB carbonated apatite unit cell parameters, mean bond lengths and polyhedral volumes calculated at the DFT/B3LYP-D* level of theory at different hydrostatic pressure conditions.

	Pressure (GPa)										
	-9.3	*-7.0*	*-4.4*	*-1.3*	*0.0*	*2.4*	*6.7*	*11.7*	*17.6*	*24.7*	*33.0*
a (Å)	9.8583	9.6698	9.5220	9.3879	9.3358	9.2580	9.1359	9.0213	8.9107	8.7987	8.7048
b (Å)	9.8069	9.6148	9.4722	9.3407	9.2926	9.2136	9.0920	8.9870	8.8536	8.7442	8.6054
c (Å)	6.9381	6.9584	6.9319	6.8905	6.8745	6.8432	6.7887	6.7251	6.6662	6.5970	6.5349
α (°)	89.54	89.59	89.62	89.67	89.68	89.99	90.35	89.11	90.80	88.94	91.36
β (°)	90.09	90.23	90.37	90.45	90.47	90.43	90.42	90.61	90.45	90.65	90.42
γ (°)	120.20	119.88	119.80	119.77	119.76	119.74	119.75	119.88	119.81	119.87	119.84
V (Å^3)	579.687	560.930	542.512	524.479	517.728	506.830	489.539	472.709	456.188	440.057	424.385
	Mean bond lengths (Å)										
< P - O >	1.5630	1.5597	1.5559	1.5516	1.5502	1.5468	1.5419	1.5370	1.5314	1.5261	1.5203
< C_A - O >	1.2999	1.2986	1.2971	1.2952	1.2944	1.2933	1.2911	1.2883	1.2858	1.2817	1.2790
< C_B - O >	1.3025	1.3008	1.2984	1.2957	1.2945	1.2930	1.2902	1.2851	1.2833	1.2770	1.2754
< Ca --- O >	2.4689	2.4705	2.4802	2.4499	2.4385	2.4216	2.4187	2.3745	2.3613	2.3286	2.3021
< Na --- O >	2.3538	2.5093	2.4473	2.3912	2.4510	2.3394	2.2916	2.3126	2.3082	2.2274	2.2298
	Polyhedral volumes (Å^3)										
< PO_4 >	1.9533	1.9418	1.9278	1.9120	1.9066	1.8944	1.8757	1.8577	1.8364	1.8169	1.7947

Table 2. Carbonate ion vibrational modes (in cm^{-1}) at different pressures, calculated at the DFT/B3LYP-D* level of theory. The values are reported as absolute variations with respect to the frequecies at 0 GPa.

CO_3^{2-} modes	**Pressure (GPa)**										
	-9.3	*-7.0*	*-4.4*	*-1.3*	*0.0*	*2.4*	*6.7*	*11.7*	*17.6*	*24.7*	*33.0*
ν_{4a} (type-A)	0	-2	-1	0	662	+2	+7	+16	+19	+36	+41
ν_{4b} (type-A)	-27	-17	-10	-3	762	+4	+11	+20	+30	+40	+53
ν_2 (type-A)	+4	+2	+1	0	887	0	-1	-2	-3	-4	-6
ν_1 (type-A)	-24	-17	-12	-2	1089	+1	+8	+20	+30	+50	+62
ν_{3a} (type-A)	-25	-16	-12	-4	1445	+4	+14	+34	+45	+73	+87
ν_{3b} (type-A)	-42	-29	-15	-4	1598	+8	+19	+29	+43	+58	+70
ν_{4a} (type-B)	-21	-16	-9	-2	694	+4	+11	+23	+27	+45	+43
ν_{4b} (type-B)	-15	-12	-7	-2	723	+3	+10	+18	+26	+33	+46
ν_2 (type-B)	+7	+4	+3	+1	875	-2	-4	-11	-8	-18	-14
ν_1 (type-B)	-34	-27	-18	-6	1097	+7	+20	+40	+48	+75	+82
ν_{3a} (type-B)	-43	-38	-24	-8	1476	+8	+23	+64	+63	+113	+111
ν_{3b} (type-B)	-33	-29	-17	-5	1548	+9	+22	+39	+56	+81	+94

Table 3. Calculated unit cell volume, isothermal bulk modulus (K_T), adiabatic bulk modulus (K_S), first derivative of bulk modulus, constant-volume (C_V) and constant-pressure (C_P) heat capacities, entropy and coefficient of volumetric thermal expansion (α_V) of type-AB carbonated apatite at 0 GPa and in the temperature range 0 K – 800 K.

T (K)	V (Å^3)	K_T (GPa)	K_S (GPa)	K'	C_V (J mol^{-1} K^{-1})	C_P (J mol^{-1} K^{-1})	S (J mol^{-1} K^{-1})	α_V (10^{-5} K^{-1})
0	521.879	103.6	103.6	4.19	0.00	0.00	0.00	0.007
10	521.879	103.7	103.7	4.19	0.59	0.59	0.09	0.010
20	521.880	103.7	103.7	4.19	8.46	8.46	2.13	0.069
30	521.883	103.7	103.7	4.19	27.57	27.57	8.12	0.195
40	521.893	103.6	103.7	4.19	57.79	57.81	18.92	0.380
50	521.913	103.6	103.7	4.19	96.12	96.18	34.66	0.592
60	521.944	103.6	103.7	4.19	138.80	138.94	54.84	0.827
70	521.987	103.5	103.7	4.19	182.69	182.95	78.62	1.059
80	522.043	103.5	103.7	4.19	225.67	226.10	105.14	1.279
90	522.109	103.4	103.7	4.19	266.56	267.20	133.62	1.479
100	522.187	103.3	103.7	4.19	304.86	305.79	163.43	1.698
150	522.710	102.9	103.5	4.18	458.69	461.52	319.20	2.414
200	523.393	102.4	103.4	4.17	567.87	573.22	470.92	2.880
250	524.183	101.9	103.2	4.15	651.00	659.31	612.66	3.216
300	525.053	101.3	103.0	4.13	717.26	728.76	744.24	3.459
350	525.987	100.8	102.8	4.12	771.14	786.28	866.58	3.681
400	526.977	100.2	102.5	4.10	815.28	834.40	980.69	3.877
450	528.018	99.6	102.3	4.08	851.60	874.96	1087.51	4.049
500	529.106	99.0	102.1	4.07	881.58	909.58	1187.83	4.215
550	530.239	98.3	101.9	4.05	906.44	939.46	1282.38	4.373
600	531.415	97.6	101.7	4.03	927.17	965.56	1371.78	4.525
650	532.634	97.0	101.5	4.02	944.54	988.58	1456.58	4.667
700	533.895	96.3	101.3	4.00	959.20	1009.61	1537.25	4.824
750	535.198	95.5	101.1	3.99	971.63	1028.46	1614.23	4.960
800	536.544	94.8	100.9	3.97	982.25	1045.69	1687.88	5.088

Table 4. Calculated unit cell volume, isothermal bulk modulus (K_T), adiabatic bulk modulus (K_S), first derivative of bulk modulus, constant-volume (C_V) and constant-pressure (C_P) heat capacities, entropy and coefficient of volumetric thermal expansion (α_V) of type-AB carbonated apatite at 300 K and in the pressure range 0 GPa – 30 GPa.

P (GPa)	V (Å^3)	K_T (GPa)	K_S (GPa)	K'	C_V (J mol^{-1} K^{-1})	C_P (J mol^{-1} K^{-1})	S (J mol^{-1} K^{-1})	α_V (10^{-5} K^{-1})
0	525.053	101.3	103.0	4.13	717.26	728.76	744.24	3.459
1	519.994	105.5	107.1	4.10	714.79	725.98	734.45	3.360
2	515.175	109.6	111.2	4.07	712.34	723.26	725.05	3.272
3	510.575	113.6	115.3	4.04	709.93	720.53	716.00	3.180
4	506.177	117.7	119.4	4.01	707.54	717.68	707.31	3.069
5	501.962	121.7	123.4	3.98	705.19	715.03	698.95	2.987
6	497.919	125.7	127.4	3.95	702.87	712.30	690.91	2.889
7	494.033	129.6	131.3	3.92	700.58	709.63	683.17	2.796
8	490.292	133.5	135.2	3.89	698.32	707.13	675.72	2.728
9	486.688	137.4	139.1	3.86	696.10	704.58	668.55	2.649
10	483.210	141.3	143.0	3.83	693.91	702.22	661.64	2.595
11	479.849	145.1	146.8	3.80	691.75	699.67	654.98	2.508
12	476.599	148.9	150.6	3.77	689.63	697.24	648.56	2.436
13	473.452	152.7	154.4	3.74	687.53	694.91	642.37	2.376
14	470.402	156.5	158.1	3.72	685.46	692.57	636.39	2.311
15	467.443	160.2	161.8	3.69	683.43	690.21	630.62	2.240
16	464.570	163.8	165.4	3.66	681.42	687.91	625.04	2.172
17	461.777	167.5	169.0	3.63	679.44	685.72	619.65	2.119
18	459.060	171.1	172.6	3.61	677.49	683.52	614.44	2.061
19	456.415	174.7	176.2	3.58	675.56	681.37	609.40	2.007
20	453.838	178.2	179.7	3.55	673.66	679.19	604.52	1.944
21	451.326	181.8	183.2	3.53	671.79	677.06	599.80	1.886
22	448.875	185.2	186.6	3.50	669.93	675.01	595.22	1.839
23	446.481	188.7	190.1	3.47	668.11	672.99	590.79	1.792
24	444.142	192.1	193.4	3.45	666.30	670.89	586.50	1.727
25	441.856	195.5	196.8	3.42	664.52	669.10	582.33	1.713
26	439.620	198.8	200.1	3.39	662.75	666.98	578.29	1.637
27	437.430	202.1	203.4	3.37	661.01	665.15	574.37	1.609
28	435.287	205.4	206.6	3.34	659.29	663.13	570.57	1.541
29	433.186	208.6	209.8	3.31	657.59	661.37	566.88	1.522
30	431.126	211.8	212.9	3.28	655.90	659.42	563.30	1.460

Figure 1

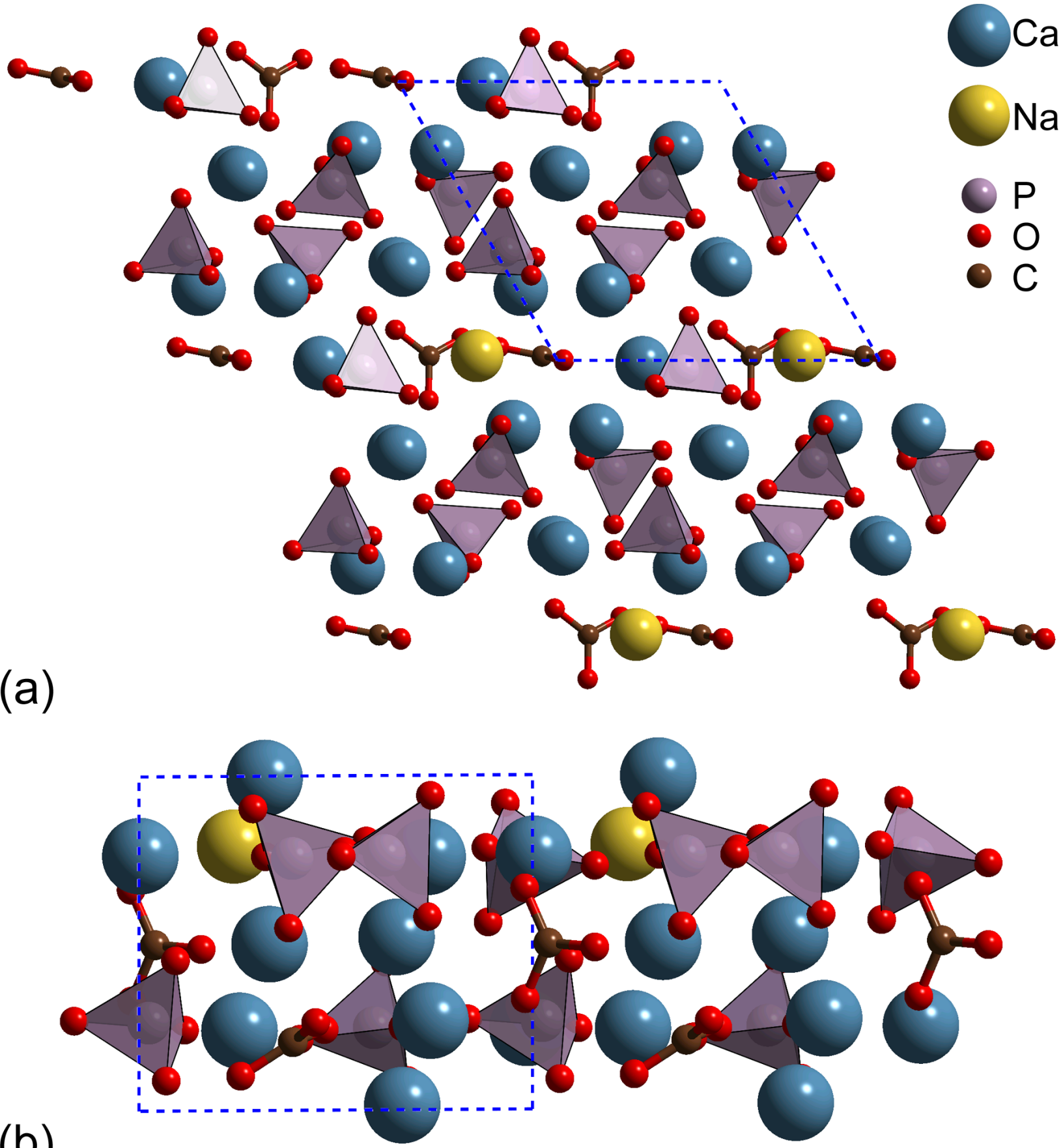

Figure 2

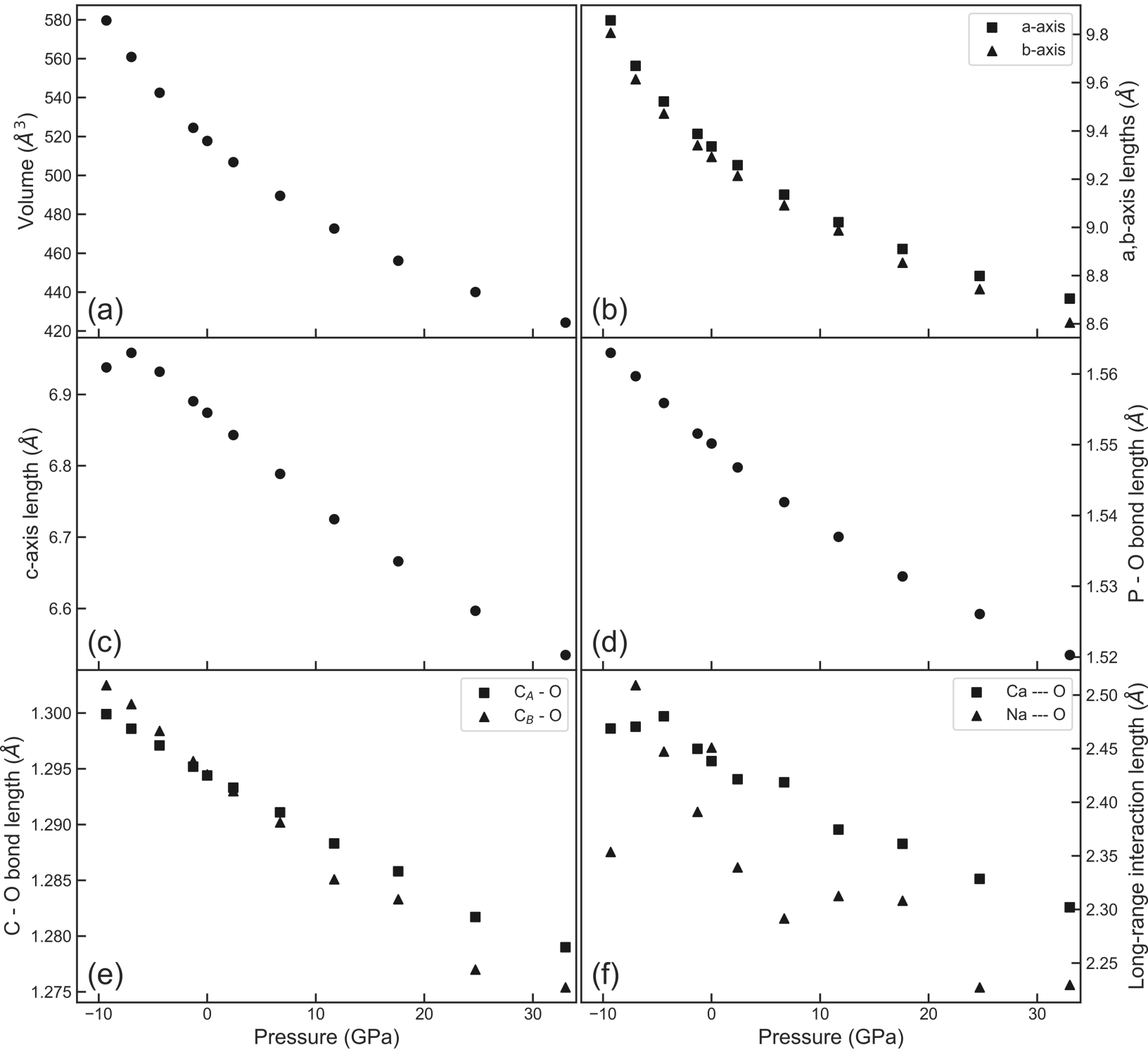
Volume (Å^3)
(a)
a-axis
b-axis
a,b-axis lengths (Å)
(b)
c-axis length (Å)
(c)
P - O bond length (Å)
(d)
C_A - O
C_B - O
C - O bond length (Å)
(e)
Ca --- O
Na --- O
Long-range interaction length (Å)
(f)
Pressure (GPa)
Pressure (GPa)

Figure 3

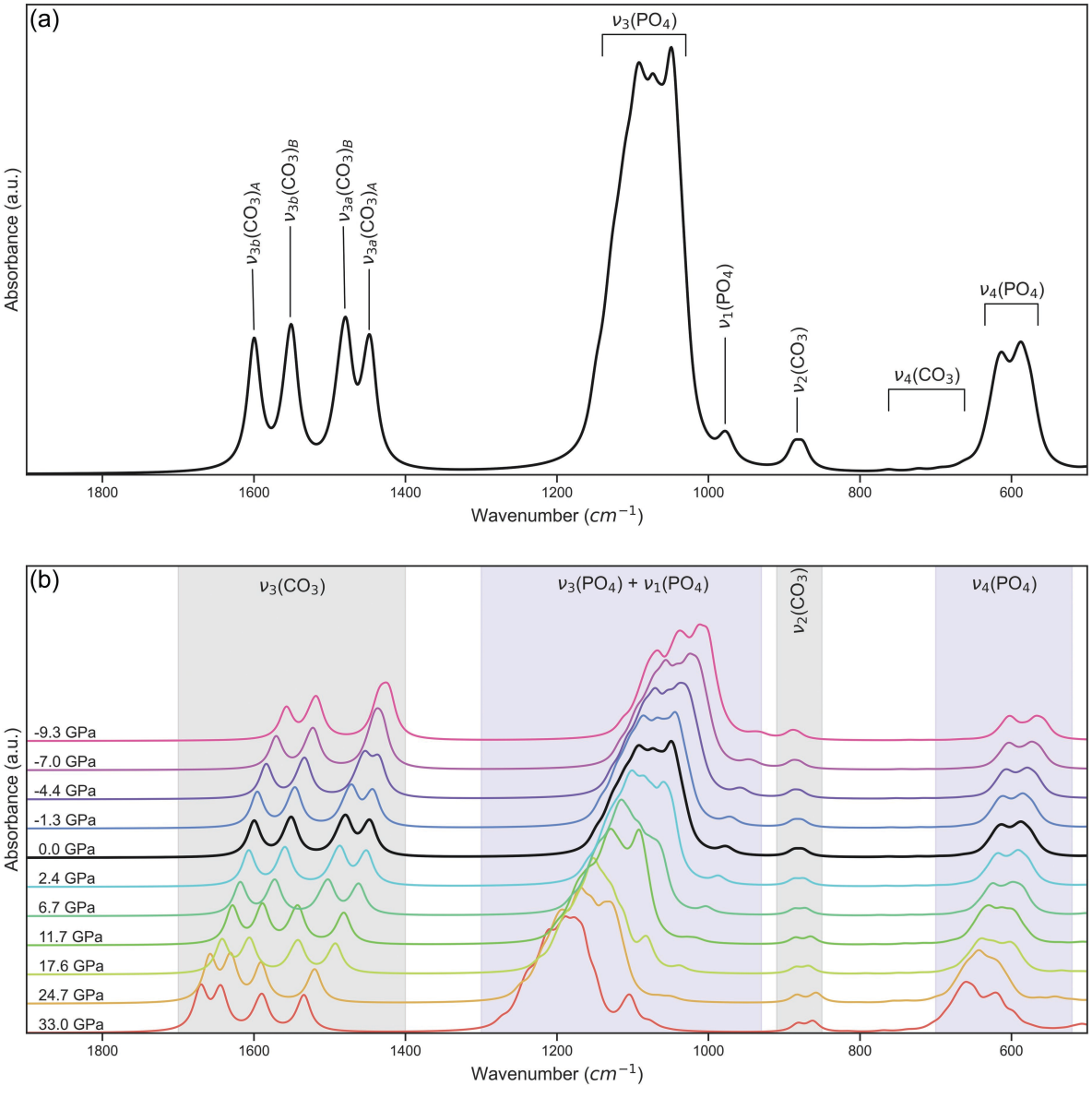
(a)
$\nu_3(PO_4)$
$\nu_{3b}(CO_3)_A$
$\nu_{3b}(CO_3)_B$
$\nu_{3a}(CO_3)_B$
$\nu_{3a}(CO_3)_A$
$\nu_1(PO_4)$
$\nu_2(CO_3)$
$\nu_4(CO_3)$
$\nu_4(PO_4)$
Absorbance (a.u.)
1800
1600
1400
1200
1000
800
600
Wavenumber (cm^{-1})
(b)
$\nu_3(CO_3)$
$\nu_3(PO_4) + \nu_1(PO_4)$
$\nu_2(CO_3)$
$\nu_4(PO_4)$
-9.3 GPa
-7.0 GPa
-4.4 GPa
-1.3 GPa
0.0 GPa
2.4 GPa
6.7 GPa
11.7 GPa
17.6 GPa
24.7 GPa
33.0 GPa
Absorbance (a.u.)
1800
1600
1400
1200
1000
800
600
Wavenumber (cm^{-1})

Figure 4a

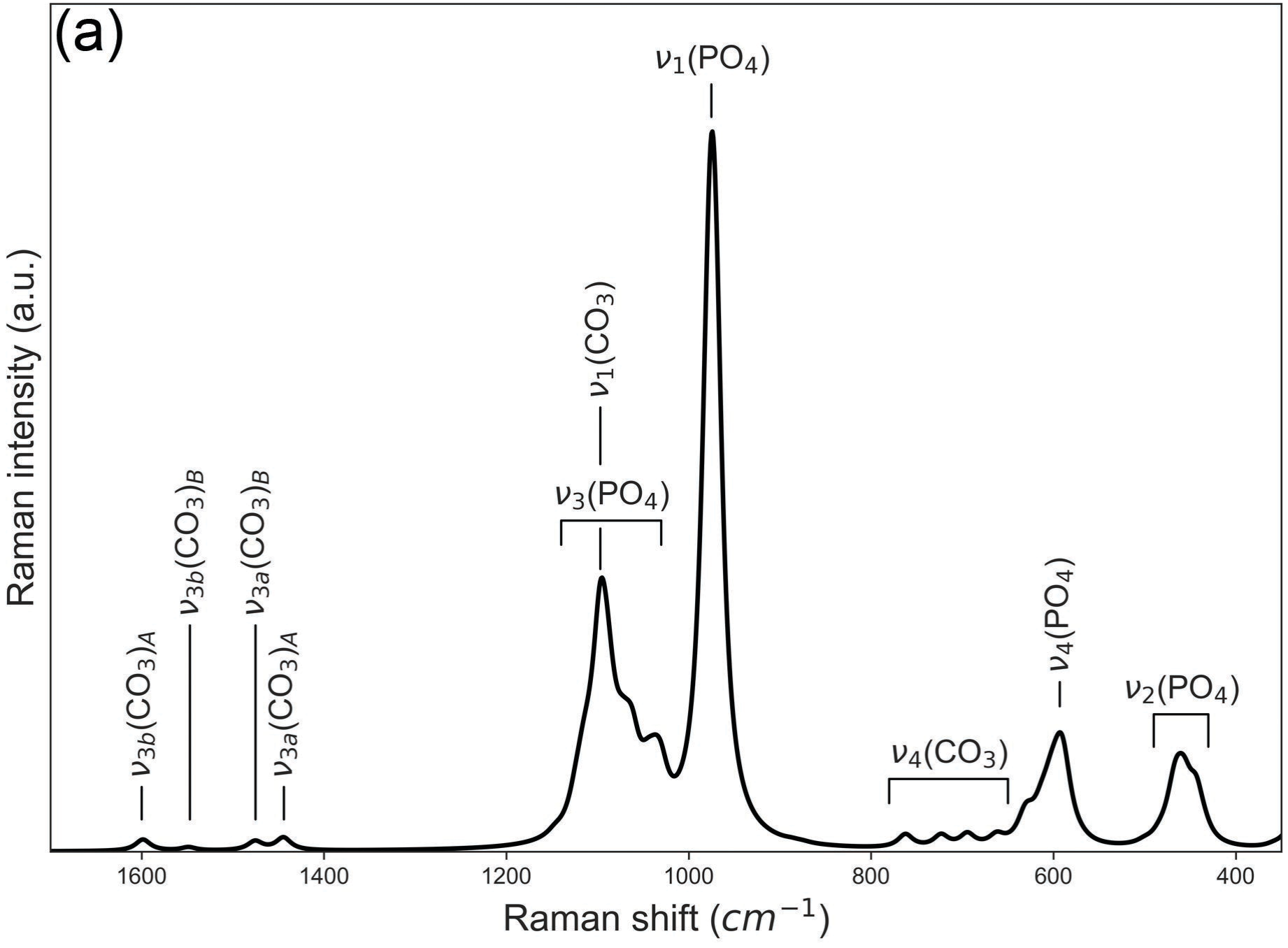
(a)
$\nu_1(PO_4)$
$\nu_1(CO_3)$
$\nu_3(PO_4)$
$\nu_{3b}(CO_3)_A$
$\nu_{3b}(CO_3)_B$
$\nu_{3a}(CO_3)_B$
$\nu_{3a}(CO_3)_A$
$\nu_4(CO_3)$
$\nu_4(PO_4)$
$\nu_2(PO_4)$
Raman intensity (a.u.)
1600
1400
1200
1000
800
600
400
Raman shift (cm^{-1})

Figure 4b

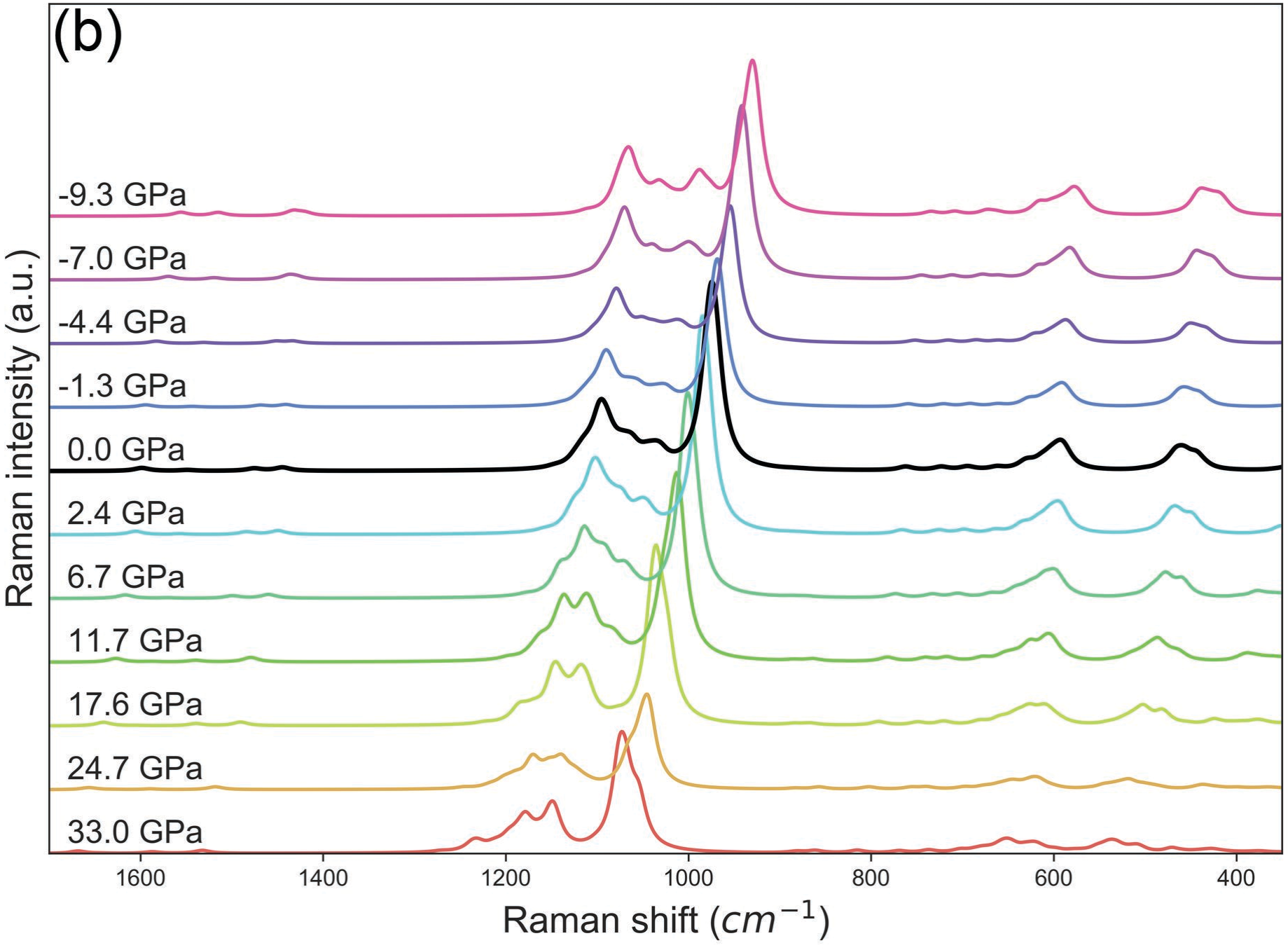
(b)
-9.3 GPa
-7.0 GPa
-4.4 GPa
-1.3 GPa
0.0 GPa
2.4 GPa
6.7 GPa
11.7 GPa
17.6 GPa
24.7 GPa
33.0 GPa
Raman intensity (a.u.)
1600
1400
1200
1000
800
600
400
Raman shift (cm^{-1})

Figure 5

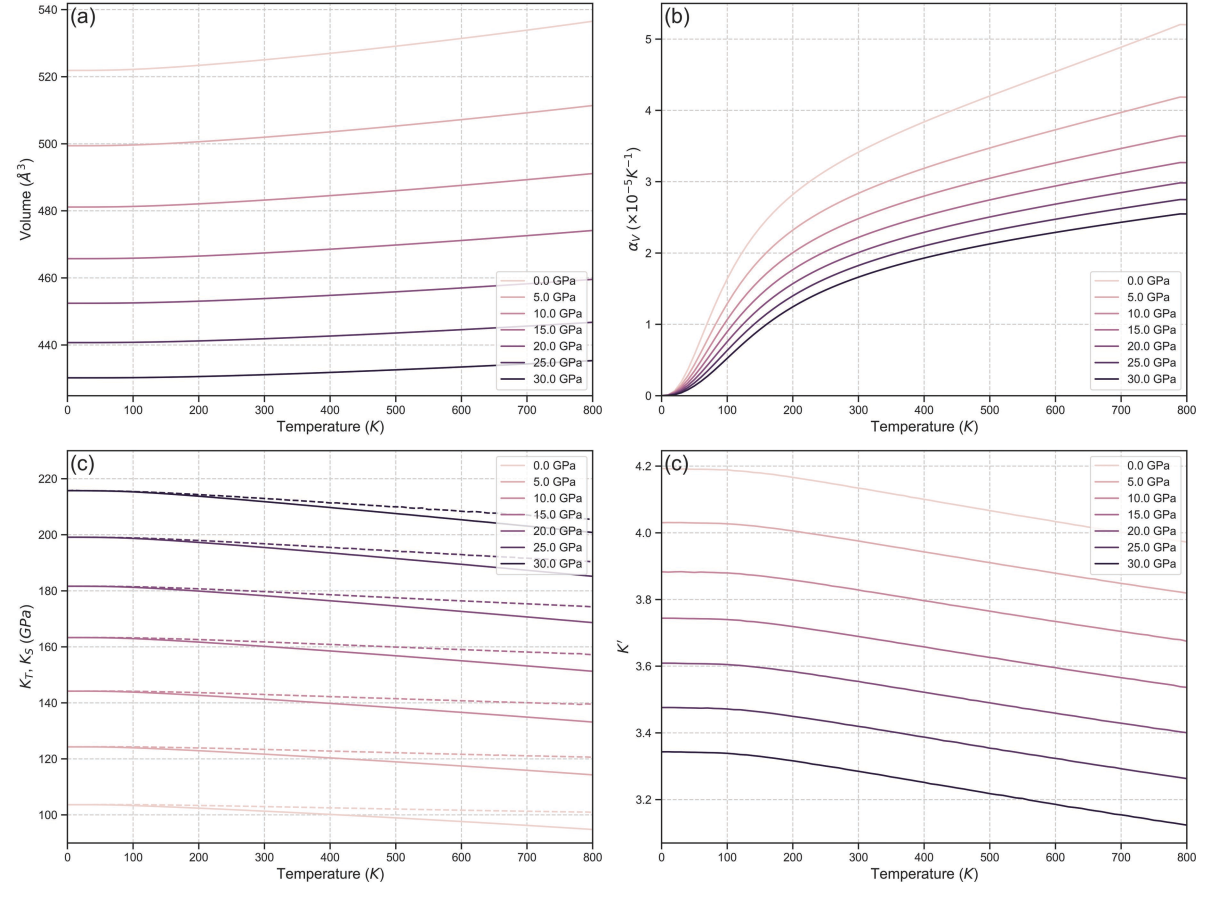
(a)
Volume ($Å^3$)
Temperature (K)
(b)
α_V ($\times 10^{-5} K^{-1}$)
Temperature (K)
(c)
K_T, K_S (GPa)
Temperature (K)
(c)
K'
Temperature (K)
0.0 GPa
5.0 GPa
10.0 GPa
15.0 GPa
20.0 GPa
25.0 GPa
30.0 GPa

Figure 6

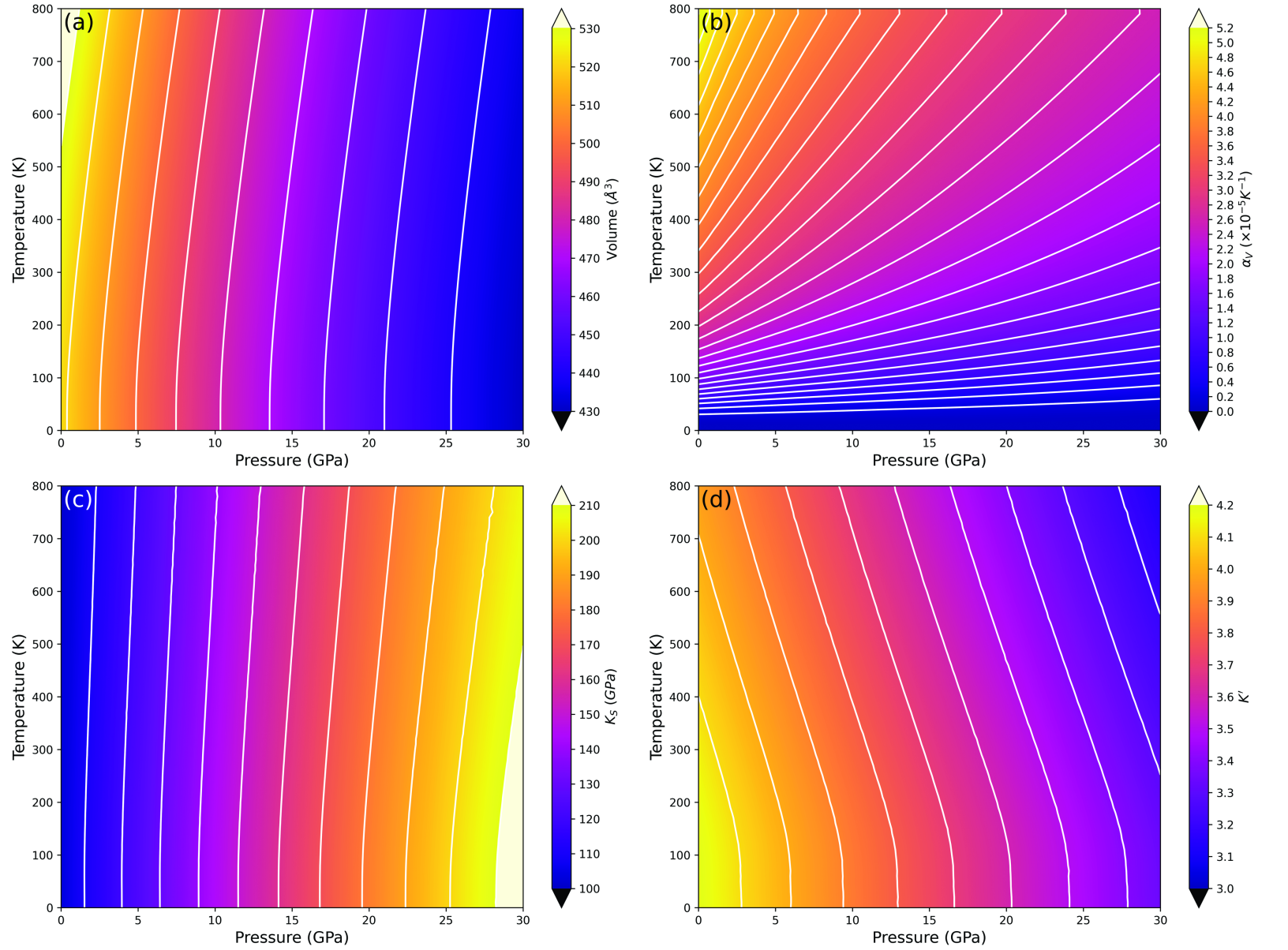
(a)
(b)
(c)
(d)
Temperature (K)
Pressure (GPa)
Volume ($Å^3$)
α_V ($\times 10^{-5} K^{-1}$)
K_S (GPa)
K'

Figure 7

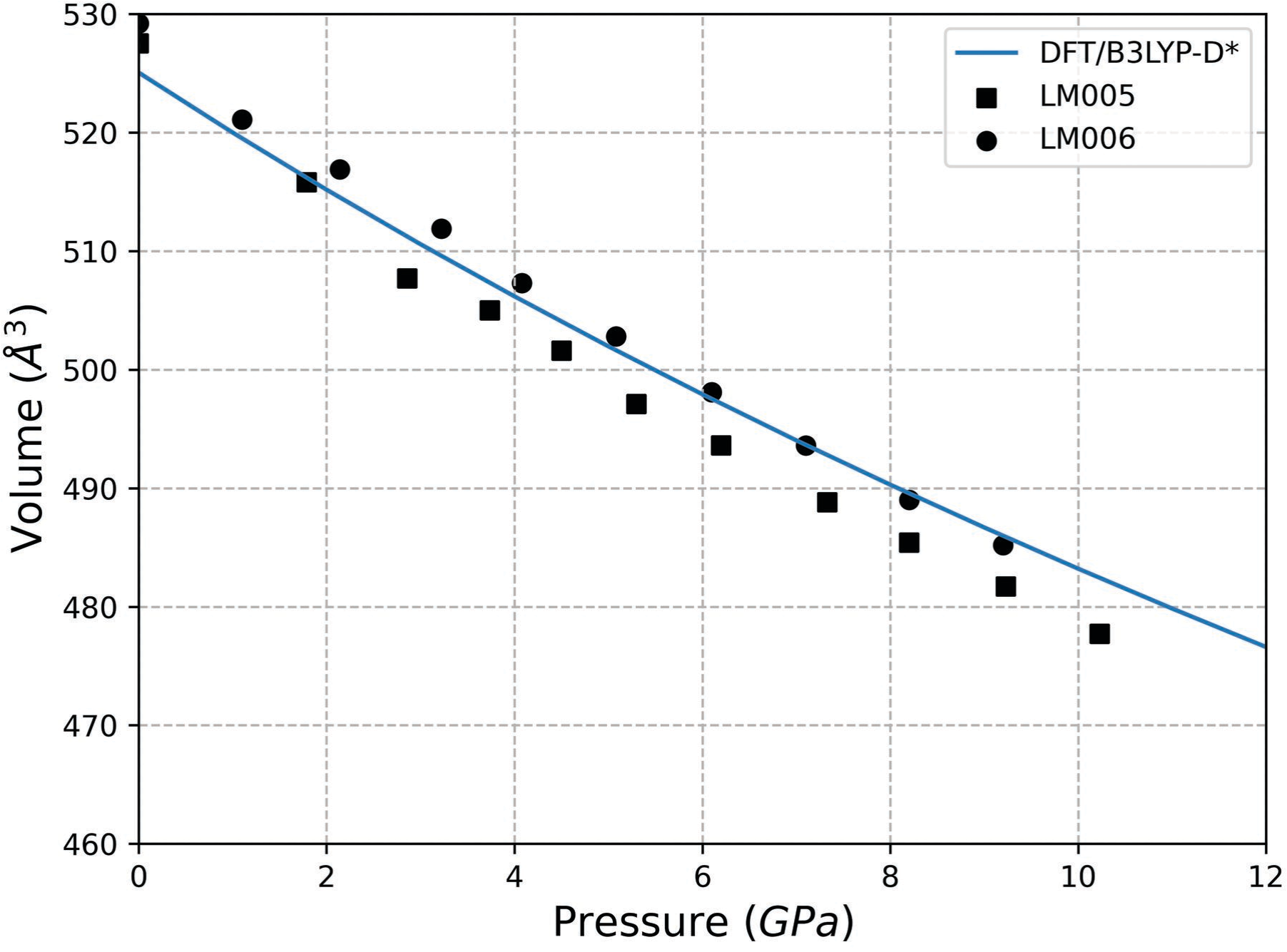
DFT/B3LYP-D*
LM005
LM006
Volume ($Å^3$)
Pressure (GPa)
530
520
510
500
490
480
470
460
0
2
4
6
8
10
12

Figure 8

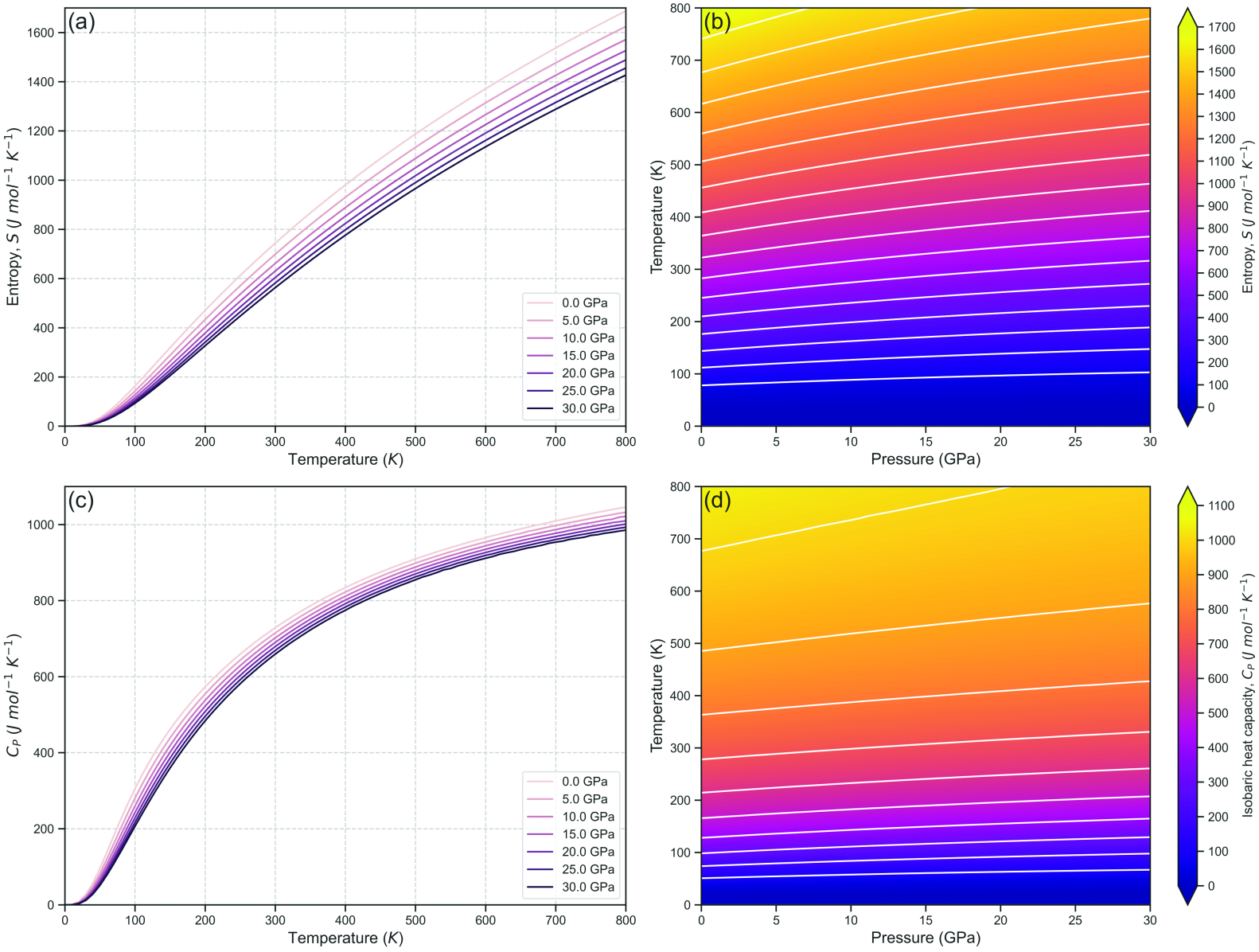
(a)
Entropy, S (J mol^{-1} K^{-1})
Temperature (K)
0.0 GPa
5.0 GPa
10.0 GPa
15.0 GPa
20.0 GPa
25.0 GPa
30.0 GPa
(b)
Temperature (K)
Pressure (GPa)
Entropy, S (J mol^{-1} K^{-1})
(c)
C_P (J mol^{-1} K^{-1})
Temperature (K)
0.0 GPa
5.0 GPa
10.0 GPa
15.0 GPa
20.0 GPa
25.0 GPa
30.0 GPa
(d)
Temperature (K)
Pressure (GPa)
Isobaric heat capacity, C_P (J mol^{-1} K^{-1})